THE ASTROPHYSICAL JOURNAL, 270:620–640, 1983 July 15

MOLECULAR CLOUDS ON THE THRESHOLD OF STAR FORMATION: THE RADIAL DENSITY PROFILE OF THE CORES OF THE RHO OPHIUCHI AND R CORONAE AUSTRALIS CLOUDS

ROBERT B. LOREN,[1] AA. SANDQVIST,[2] AND A. WOOTTEN[3,4]
Received 1982 June 29; accepted 1982 December 22

ABSTRACT

In a cold, dense, dynamically evolved cloud core that lacks embedded massive stars, the density distribution should reflect a stage of cloud evolution at the threshold of star formation. The radial density distribution in three such dense massive cores, located within two nearby regions of recent star formation, has been determined from extensive maps of two H_2CO transitions. The appearance of the maps of emission and absorption of the 2 cm line confirms the predictions of models for the excitation of this transition. Detailed models of the H_2CO radiative transport demonstrate that a rapid radial decline of density, $\rho(R) \propto R^{-3/2}$ to R^{-2}, from a density of 10^6 cm^{-3} in the core to 10^4 cm^{-3} in the envelope, occurs over radial distances from 0.06 to 0.60 pc. These models require a decline in H_2CO abundance with increasing density in these cold cores, perhaps a result of condensation of gas onto grains. For the observed values of core radius (0.06–0.09 pc) and core mass (19–110 $M_\odot$), the H_2CO line widths indicate that the velocity dispersion due to rotation or turbulence is too small to stabilize the cloud against gravitational collapse. The observed magnetic field strength also appears to be inadequate to prevent cloud contraction and eventual star formation.

The unusual 2 cm H_2CO emission toward ρ Oph B is found to be spatially extended ($8' \times 4'$). The lack of far-infrared emission from this cold dense ($> 10^6$ cm^{-3}) region indicates a lack of stars of high luminosity embedded within or near the surface of the cloud. The combination of cold, very dense gas in a centrally condensed region together with a lack of internal support means that within ρ Oph B the stage has been set for the possible formation of one or more massive protostars.

Subject headings: interstellar: molecules — nebulae: individual — stars: formation

I. INTRODUCTION

Determining the physical conditions which lead to star formation is one of the principal goals of interstellar millimeter molecular spectroscopy. The birth of a massive star rapidly disrupts the cloud from which it formed. The high radiative and stellar wind output of a massive star will alter the temperature and velocity structure that we observe. The ionization levels and the radial variation of chemical abundances will also be changed on a rapid time scale. Even in the youngest observed star formation regions these physical properties may no longer reflect the conditions which existed prior to star formation, since even low-mass young stars have stellar winds which can alter the velocity structure of the surrounding cloud (Snell, Loren, and Plambeck 1980). The radial density profile of a cloud is one physical parameter which requires a longer time scale to be altered after the onset of star formation. We will determine the density distribution toward very dense cores in clouds in which nearby star formation has so far been limited to low-mass stars which do not totally disrupt the cloud. We examine the stability of these dense cores to further gravitational collapse that could lead to formation of additional stars.

Molecular spectral lines provide convenient probes of density when they are modeled with the collisional excitation required to produce the observed line intensities. Recent studies have used CO (Plambeck and Williams 1979), NH_3 (Ho 1977), CS (Linke and Goldsmith 1980), and H_2CO (Evans and Kutner 1976; Wootten *et al.* 1978; Wooten, Snell, and Evans 1980; Loren, Evans, and Knapp 1979) as density probes. More recently, using the lower abundance isotopic species DCO^+ and $H^{13}CO^+$ as density probes (Wootten, Loren, and Snell 1982; Loren *et al.* 1983), the potential problems of line saturation have been reduced. These surveys have typically considered only a single position at the dense core of a number of clouds. Some limited mapping of density

[1]Millimeter Wave Observatory, McDonald Observatory, and the Electrical Engineering Research Laboratory, The University of Texas at Austin.
[2]Stockholm Observatory, Saltsjöbaden, Sweden.
[3]Department of Physics, Rensselaer Polytechnic Institute.
[4]Owens Valley Radio Observatory, California Institute of Technology.

determined from H_2CO toward a few clouds was presented by Loren, Evans, and Knapp (1979), Wootten, Snell, and Evans (1980), and Sandqvist and Bernes (1980).

The dynamical evolution of a molecular cloud—its collapse to form stars—will leave its imprint upon the cloud's density distribution. To obtain the density distribution requires a determination of the cloud density at multiple radial positions. Many molecular lines are detectable only in a high-density core and not in the surrounding lower density envelope. Because of its high abundance and the easy accessibility of a number of transitions, excited at a variety of densities, formaldehyde (H_2CO) is ideally suited for the study of both the high-density core and the surrounding lower density envelope.

It is generally difficult to establish the density profile of most high-density molecular clouds since the spatial resolution achieved at their large distances is poor. To obtain the highest spatial resolution we have selected two nearby molecular clouds (distance ~ 150 pc) which contain high-density cores but have formed mostly low-mass stars: the ρ Oph and R CrA molecular clouds. We have mapped two transitions of H_2CO over many beamwidths in each of these clouds. Within the ρ Oph cloud two separate dense cores, designated ρ Oph A and ρ Oph B, were found.

The two H_2CO lines that we observed are the $J_{K_{-1}K_1} = 2_{12}-2_{11}$ transition at 14.488479 GHz (hereafter referred to as the 2 cm transition) and the $J_{K_{-1}K_1} = 2_{12}-1_{11}$ transition at 140.839535 GHz (hereafter referred to as the 2 mm transition). Comparison of the intensity of these two lines with calculated models allows us to establish the density at a large number of positions in each cloud.

The beam sizes of the two telescopes used are nearly the same at the frequencies of the two observed H_2CO lines, so regions of the same projected area are being compared. The two observed transitions arise from the same state (2_{12}), which ensures that the lines are excited at roughly the same density, and thus sample the same volume of space. When the density becomes high enough ($\sim 10^4$ cm^{-3}) to populate the 2_{12} level, the 2 mm line will appear weakly in emission, and the 2 cm line will at first appear in absorption. While the 2 mm line intensity continues to increase with increasing density, the 2 cm line reaches a maximum absorption strength and then weakens, finally going into emission at very high densities ($\gtrsim 10^6$ cm^{-3}). This decrease of 2 cm absorption strength and the transition from absorption to emission that occurs for all temperatures at a density of $\sim 10^6$ cm^{-3} are unique predictions of the H_2CO excitation models, the confirmation of which is completely independent of line strength calibration. Detection of the 2 cm H_2CO line in emission is rare, and its detection in the ρ Oph B cloud represents the coldest of the known regions of 2 cm emission (Loren *et al.* 1980). The range over which the observed transitions of H_2CO are a useful density probe is roughly two orders of magnitude (10^4–10^6 cm^{-3}). This is an important attribute for a density probe in nearby clouds with large density variations such as ρ Oph or R CrA (Loren, Evans, and Knapp 1979). The H_2CO observations are presented in § II, and the density models of H_2CO are discussed in § III. The radial density distribution is determined in § IV for the ρ Oph cloud along with a comparison of the H_2CO distribution with other molecular probes. The radial density distribution toward the R CrA cloud is determined in § V. A comparison of the observed density distribution with that calculated from models of the collapse of a cloud to form a protostar is used to discuss the evolutionary state of these clouds in § VI.

II. OBSERVATIONS

The 2 cm H_2CO line was observed with the NRAO[5] 43 m antenna at Green Bank, West Virginia. The beam size was 2′ at 14.49 GHz, and a velocity resolution of 0.27 km s^{-1} was achieved with an autocorrelation spectrometer. Corrections have been made to the 2 cm data to account for measured changes in beam efficiency (η_B) with elevation (Loren, Evans, and Knapp 1979). The intensities are expressed as $T_B = T_A/\eta_B$. Because both observed clouds are at low declination ($-24°$ and $-37°$) and can be tracked only at low elevations, we limited the observations to an elevation range of 22°–27° for ρ Oph and 12°–15° for R CrA. In this case the dominant error in the efficiency correction will be that due to poorly known azimuthal variations. At an elevation of 25° appropriate to ρ Oph, $\eta_B = 0.30$, while at an elevation of 15° appropriate to R CrA, $\eta_B = 0.24$. A change in the axial configuration of the receiver package on the 43 m antenna between sets of 2 cm observations complicates calibration. However, similar line profiles and intensities were obtained toward the same sky position with the different receiver configurations, indicating that these changes have not seriously affected our calibration.

The 2 mm H_2CO line was observed with the Millimeter Wave Observatory (MWO)[6] 4.9 m antenna at Ft. Davis, Texas. The beam size at 140.8 GHz was 1′.8, and the data were obtained with velocity resolutions of 0.53 km s^{-1} and 0.13 km s^{-1}. The intensities are expressed as $T_R^* = T_A^*/\eta_{FSS}$, which corrects T_A^* for the forward scattering and spillover losses ($\eta_{FSS} = 0.83$).

[5]The National Radio Astronomy Observatory is operated by Associated Universities, Inc., under contract with the National Science Foundation.

[6]The Millimeter Wave Observatory is operated by the Electrical Engineering Research Laboratory of The University of Texas at Austin, with support from the National Science Foundation and McDonald Observatory.

TABLE 1

ρ OPH A H_2CO

	Position	2 Centimeter T_A	V_{LSR}	ΔV	rms	T_B	2 Millimeter T_A^*	V_{LSR}	ΔV	rms	T_R^*	$\langle T_B$ (2 cm)$\rangle$	$\langle T_R^*$ (2 mm)$\rangle$	R_θ (′)	R (pc)	$\langle T_R^*$(CO)$\rangle$
A1	ON	< -0.03	...	...	0.016	< -0.10	2.5	3.3	1.1	0.2	2.9					
	2W	-0.07	3.7	2.0	0.03	-0.24	1.9	3.3	1.1	0.3	2.2	-0.12 ± 0.08	2.5 ± 0.5	1.4	0.06	40
	2S − 2W	≤ -0.02	3.6	2.8	0.016	≤ -0.07	2.4	2.8	1.4	0.4	2.8					
	2S	< -0.02	...	...	0.015	< -0.07	1.6	2.8	1.6	0.3	1.9					
A2	2N	-0.11	3.4	1.1	0.04	-0.34	1.2	3.3	1.5	0.3	1.4					
	2N − 2W	-0.11	3.3	1.5	0.03	-0.40	1.6	3.0	2.2	0.2	1.9					
	4W	-0.09	3.1	1.6	0.02	-0.30	1.1	2.8	2.7	0.3	1.3					
	2S − 4W	-0.05	3.4	1.1	0.03	-0.16	1.7	2.8	1.5	0.3	2.0					
	4S − 2W	≤ -0.07	4.2?	0.5	0.04	≤ -0.23	1.5	3.2	1.0	0.3	1.8	-0.22 ± 0.12	1.4 ± 0.5	3.2	0.14	40
	4S	≤ -0.05	3.1	1.2	0.025	≤ -0.16	0.9	3.8	1.7	0.3	1.1					
	2S − 2E	< -0.03	...	...	0.02	< -0.10	1.2	2.8	2.0	0.2	1.4					
	2E	-0.02	3.4	1.8	0.014	-0.08	0.5	3.8	0.8	0.2	0.6					
A3	2N − 4W	-0.10	3.1	1.3	0.04	-0.32	1.5	2.6	1.7	0.2	1.8					
	4S − 4W	< 0.10	...	...	0.05	< -0.32	0.6	3.8	1.5	0.3	0.7	-0.29 ± 0.06	1.1 ± 0.6	4.2	0.19	40
	4S − 2E	-0.09	3.4	0.6	0.03	-0.33	1.2	2.8	1.6	0.2	1.4					
	2N − 2E	-0.06	3.5	1.1	0.03	-0.22	0.35	3.1	1.5	0.2	0.4					
A4	4N	-0.11	3.5	0.7	0.03	-0.35	0.45	3.3	1.5	0.2	0.5					
	4N − 2W	-0.08	3.0	1.4	0.03	-0.28	0.55	2.6	2.4	0.2	0.65					
	6W	-0.08	3.4	0.9	0.025	-0.28	1.05	3.0	2.6	0.3	1.2					
	2S − 6W	-0.04	2.8	0.8	0.02	-0.12	0.8	2.8	1.0	0.2	0.9	-0.25 ± 0.09	0.9 ± 0.3	5.1	0.22	40
	6S − 2W	< -0.08	...	...	0.04	< -0.28	0.7	3.0	2.6	0.2	0.8					
	6S	...	...	...	...	...	0.7	2.9	1.8	0.2	0.8					
	2S − 4E	-0.10	3.3	0.8	0.03	-0.31	1.3	3.4	1.5	0.2	1.5					
	4E	-0.04	3.1	2.3	0.03	-0.14	0.8	3.2	1.0	0.2	0.9					
A5	4N − 4W	-0.05	3.1	2.0	0.03	-0.20	0.8	3.0	1.8	0.2	0.9					
	2N − 6W	-0.06	2.9	2.4	0.02	-0.20	0.8	2.8	1.8	0.2	0.9					
	4S − 6W	...	...	...	...	...	...	...	...	...	...					
	6S − 4W	...	...	...	...	...	≤ 0.5	2.2	1.5	0.2	≤ 0.6					
	6S − 2E	-0.07	4.0	1.5	0.03	-0.24	0.8	3.0	2.0	0.2	0.9	-0.22 ± 0.07	0.8 ± 0.4	5.8	0.25	35
	4S − 4E	-0.10	3.8	0.7	0.02	-0.30	1.3	3.2	0.9	0.3	1.5					
	2N − 4E	-0.03	2.7	0.6	0.02	-0.10	< 0.2	...	...	0.1	< 0.24					
	4N − 2E	-0.08	3.5	0.7	0.03	-0.26	< 0.5	...	...	0.2	0.6					
A6	6N	-0.04	2.9	1.4	0.015	-0.15	≤ 0.4	3.8	2.6	0.2	0.5					
	4N − 6W	-0.08	3.5	1.2	0.03	-0.27	0.7	3.4	1.4	0.3	0.8	-0.23 ± 0.07	0.65 ± 0.25	7.1	0.31	30
	6S − 6W	< -0.08	...	...	0.03	< -0.27	...	...	...	...	...					
A7	2N − 6E	< -0.05	...	...	0.04	< -0.16	...	...	...	...	...	...	...	7.6	0.33	30
A8	6N − 6W	-0.04	3.2	1.1	0.02	-0.13	0.3	3.0	1.9	0.2	0.35	-0.13	0.35	8.6	0.37	25

TABLE 2

ρ OPH B H_2CO

Position		2 Centimeter T_A	V_{LSR}	ΔV	rms	T_B	2 Millimeter T_A^*	V_{LSR}	ΔV	rms	T_R^*	$\langle T_B$ (2 cm)$\rangle$	$\langle T_R^*$ (2 mm)$\rangle$	R_θ (′)	R (pc)	$\langle T_R^*$ (CO)$\rangle$
B1	4S−12E.....	+0.07	3.3	1.0	0.03	+0.23	1.3	3.5	1.9	0.3	1.5					
	4S−10E.....	−0.02	3.6	1.1	0.02	−0.10	1.3	3.2	1.8	0.2	1.5	+0.17±0.18	1.8±0.3	1.4	0.06	30
	6S−10E.....	+0.09	3.5	1.0	0.02	+0.30	1.8	3.1	1.2	0.2	2.1					
	6S−12E.....	+0.08	3.5	1.1	0.02	+0.26	1.7	3.2	1.9	0.2	2.0					
B2	2S−12E.....	+0.08	2.9	0.7	0.02	+0.26	1.4	3.2	1.4	0.2	1.65					
	2S−10E.....	< −0.04	...	...	0.02	< −0.13	1.0	3.2	1.6	0.2	1.2					
	4S−8E.....	−0.11	3.6	0.8	0.03	−0.36	1.3	3.2	1.8	0.3	1.5					
	6S−8E.....	< 0.06	...	...	0.03	< ±0.17	1.3	3.2	1.3	0.2	1.5					
	8S−10E.....	+0.17	3.5	0.8	0.02	+0.54	1.3	3.3	1.5	0.3	...	+0.08±0.27	1.4+0.2	3.2	0.14	30
	8S−12E.....	+0.07	3.5	1.0	0.03	+0.23	1.3	3.5	1.5	0.3	1.5					
	6S−14E.....	< 0.08	...	...	0.04	< ±0.22	1.0	3.5	2.7	0.2	1.2					
	4S−14E	+0.05	3.2	1.5	0.02	+0.17	1.3	3.5	2.2	0.3	1.5					
B3	2S−8E.....	−0.06	3.2	0.6	0.02	−0.20	0.7	3.6	1.1	0.2	0.8					
	8S−8E.....	< −0.05	...	...	0.03	< −0.17	1.3	3.8	1.3	0.3	1.5	−0.16±0.04	1.3±0.4	4.2	0.19	25
	8S−14E.....	−0.05	...	...	0.02	−0.17	0.9	3.8	1.5	0.2	1.1					
	2S−14E.....	≤ −0.03	3.9	1.0	0.02	≤ −0.10	1.4	3.3	1.3	0.2	1.65					
B4	12E.....	−0.06	3.3	1.2	0.02	−0.20	1.0	3.2	1.1	0.25	1.2					
	10E.....	−0.06	3.3	0.9	0.02	−0.20	0.45	3.7	1.1	0.2	0.55					
	4S−6E.....	−0.07	3.6	1.0	0.02	−0.23	1.3	3.2	1.3	0.3	1.5					
	6S−6E.....	−0.08	3.5	2.0	0.03	−0.26	0.7	2.7	1.8	0.2	0.8	−0.21±0.06	1.0±0.35	5.1	0.22	25
	10S−10E	−0.09	3.0	0.7	0.03	−0.30	0.9	3.5	1.0	0.3	1.1					
	10S−12E	−0.035	3.7	1.8	0.03	−0.12	0.8	3.2	1.5	0.2	0.9					
	6S−16E.....	...	...	...	...	...	0.4	3.7	1.4	0.2	0.5					
	4S−16E.....	< −0.05	...	...	0.02	< −0.17	1.0	3.2	2.2	0.3	1.2					
B5	2S−6E	−0.06	3.8	0.7	0.02	−0.20	0.6	2.7	3.6	0.2	0.7					
	8S−6E.....	−0.05	3.0	2.0	0.02	−0.17	1.0	3.6	1.6	0.2	1.2					
	10S−8E.....	−0.07	3.5	1.5	0.02	−0.23	1.1	3.8	2.0	0.3	1.3					
	10S−14E	−0.08	3.5	1.1	0.03	−0.26	0.6	3.7	1.1	0.2	0.7					
	8S−16E.....	−0.06	3.3	1.0	0.02	−0.20	≤ 0.4	3.8	1.1	0.2	≤ 0.5	−0.21±0.03	0.85±0.3	5.8	0.25	30
	2S−16E.....	...	...	...	...	...	0.7	3.7	1.5	0.2	0.8					
	14E.....	≤ −0.06	3.1	0.3	0.02	≤ −0.20	0.65	3.2	1.1	0.2	0.75					
	8E.....	...	...	...	...	...	...	...	...	...	...					
B6	6S−4E.....	−0.11	3.4	0.7	0.02	−0.36	1.0	3.1	1.4	0.3	1.2					
	10S−6E.....	−0.09	3.4	1.5	0.02	−0.30	1.0	3.3	1.6	0.2	1.2	−0.33±0.03	0.9±0.5	7.1	0.31	30
	12S−12E	−0.10	3.4	1.0	0.02	−0.33	≤ 0.3	3.2	1.2	0.15	≤ 0.4					
B7	8S−4E.....	−0.09	3.6	1.7	0.04	−0.30	0.6	3.9	0.9	0.2	0.7					
	12S−8E.....	−0.09	3.6	1.9	0.02	−0.30	0.7	3.7	1.1	0.2	0.8	−0.30	0.75±0.1	7.6	0.33	30
B8	12S−16E....	−0.07	3.1	0.7	0.02	−0.23	0.45	3.4	1.1	0.15	0.55	−0.23	0.55	8.6	0.37	20
B9	12S−4E.....	−0.065	3.4	1.4	0.02	−0.21	0.9	3.3	0.9	0.3	1.1	−0.21	1.1	9.9	0.43	30
B10	E29.....	−0.07	3.8	2.3	0.02	−0.23	0.6	4.9	1.1	0.2	0.7	−0.23	0.7	10.1	0.44	25

TABLE 3

R CrA H_2CO

		2 Centimeter					2 Millimeter									
	Position	T_A	V_{LSR}	ΔV	rms	T_B	T_A^*	V_{LSR}	ΔV	rms	T_R^*	$\langle T_B$ (2 cm)$\rangle$	$\langle T_R^*$ (2 mm)$\rangle$	R_θ (′)	R (pc)	$\langle T_R^*$ (CO)$\rangle$
C0	ON	< −0.02	...	...	0.013	< −0.07	2.6	5.7	1.6	0.4	3.1	≤ −0.07	3.1	0	0	25
C1	2N	−0.03	5.5	2.7	0.02	−0.14	1.0	5.5	1.6	0.3	1.2					
	2W	−0.07	6.0	1.2	0.02	−0.32	1.8	6.2	1.5	0.7	2.1	−0.24 ± 0.12	1.9 ± 0.6	2	0.09	20
	2S	< −0.06	...	...	0.03	−0.14	2.2	6.2	0.9	0.7	2.6					
	2E	−0.08	5.6	1.4	0.02	−0.36	1.3	6.2	1.2	0.4	1.5					
C2	2N − 2W	−0.04	5.5	1.5	0.02	−0.19	1.7	5.3	1.6	0.7	2.0					
	2S − 2W	−0.06	5.6	0.9	0.02	−0.27	0.6	5.7	1.1	0.2	0.7	−0.21 ± 0.05	1.6 ± 0.7	2.8	0.12	20
	2S − 2E	−0.03	6.0	2.0	0.02	−0.14	1.8	6.3	1.0	0.5	2.1					
	2N − 2E	−0.05	5.6	1.2	0.02	−0.22	1.2	5.6	0.7	0.4	1.4					
C3	4N	−0.05	5.0	1.3	0.03	−0.23	0.8	5.1	1.0	0.4	0.9					
	4W	−0.07	5.7	1.0	0.03	−0.33	1.3	6.2	1.6	0.5	1.5	−0.33 ± 0.12	1.4 ± 0.4	4	0.18	20
	4S	−0.11	6.3	0.4	0.03	−0.50	1.5	5.8	1.2	0.6	1.8					
	4E	−0.06	4.8?	1.1	0.03	−0.25	1.1	6.3	1.8	0.5	1.3					
C4	4N − 2W	−0.06	5.5	0.6	0.02	−0.25	1.7	5.8	1.6	0.6	2.0					
	2N − 4W	−0.07	5.8	1.4	0.02	−0.32	1.5	6.2	1.0	0.5	1.8					
	2S − 4W	−0.10	5.7	0.4	0.02	−0.46	≤ 0.5	5.8	...	0.3	≤ 0.6					
	4S − 2W	−0.06	5.9	1.7	0.03	−0.27	0.3	5.8	1.6	0.2	0.35	−0.32 ± 0.09	1.4 ± 0.8	4.5	0.20	20
	4S − 2E	−0.09	6.0	0.9	0.02	−0.41	2.0	6.3	1.5	0.8	2.4					
	2S − 4E	−0.06	5.9	2.3	0.02	−0.27	1.9	6.1	1.1	0.6	2.2					
	2N − 4E	−0.04	5.4	0.6	0.02	−0.18	0.9	5.4	1.8	0.3	1.1					
	4N − 2E	< −0.08	...	...	0.04	−0.36	0.4	4.3?	1.8	0.2	0.5					
C5	4N − 4W	−0.07	5.6	1.3	0.02	−0.31	1.7	6.3	1.1	0.6	2.0					
	4S − 4W	< −0.05	...	...	0.03	< −0.22	1.5	6.2	0.8	0.5	1.8	−0.22 ± 0.07	1.5 ± 0.6	5.7	0.25	20
	4S − 4E	−0.05	6.0	1.1	0.03	−0.20	1.5	6.2	0.8	0.5	1.8					
	4N − 4E	≤ −0.03	5.4	1.7	0.02	≤ −0.14	0.5	6.2	0.7	0.2	0.6					
C6	6N	< −0.06	...	...	0.03	−0.27	≤ 0.3	5.6	...	0.2	≤ 0.35					
	6W	−0.04	6.3	0.8	0.02	−0.20	< 0.3	...	...	0.2	< 0.35	−0.23 ± 0.05	0.6 ± 0.3	6	0.27	20
	6S	< −0.04	...	...	0.03	< −0.18	< 0.5	...	...	0.2	< 0.6					
	6E	−0.06	5.7	1.3	0.03	−0.27	0.8	6.2	0.8	0.3	0.9					
C7	6N − 2W	−0.07	5.7	1.1	0.03	−0.33	0.8	6.2	0.7	0.3	0.9					
	2N − 6W	−0.05	5.5	0.4?	0.02	−0.22	0.7	6.3	1.1	0.3	0.8	−0.32 ± 0.15	1.0 ± 0.2	6.3	0.28	25
	6S − 2E	−0.11	5.9	0.3	0.02	−0.53	1.0	6.2	0.7	0.3	1.2					
	2S − 6E	−0.04	5.2	1.6	0.03	−0.19	0.9	5.7	2.2	0.4	1.1					
C8	6N − 4W	−0.03	5.1	1.5	0.03	−0.14	< 0.4	...	...	0.3	< 0.5	−0.25 ± 0.16	0.8 ± 0.4	7.2	0.32	25
	4N − 6W	−0.08	5.6	1.6	0.03	−0.36	0.9	6.1	1.2	0.4	1.1					
C9	8E	≤ −0.05	5.3	0.3	0.03	≤ −0.23	0.4	5.9	2.6	0.2	0.5					
	6S − 6E	−0.05	5.7	3.8	0.02	−0.23	0.8	6.2	0.6	0.3	0.9					
	4N − 8W	−0.03	6.0	0.8	0.02	−0.15	0.6	6.0	1.1	0.2	0.7	−0.19 ± 0.04	0.75 ± 0.3	⟨8.6⟩	0.38	20
	8S − 4E	< −0.04	...	...	0.04	< −0.18	< 0.4	...	...	0.3	< 0.5					
	4S − 8E	−0.04	5.5	0.7	0.02	−0.16	1.0	5.7	1.2	0.2	1.2					
C10	2N − 10W	−0.07	6.2	1.0	0.03	−0.33	0.7	6.1	1.0	0.3	0.8					
	8S − 8E	−0.05	5.9	0.8	0.02	−0.22	0.35	5.7	0.6	0.15	0.4	−0.30 ± 0.06	0.5 ± 0.2	⟨11.2⟩	0.50	20
	10S − 6E	−0.06	5.4	0.9	0.02	−0.27	0.35	6.2	1.1	0.1	0.4					
	6S − 10E	−0.08	5.7	0.6	0.03	−0.36	< 0.4	...	...	0.2	< 0.5					
C11	10S − 10E	−0.08	5.7	0.7	0.02	−0.39	< 0.4	...	...	0.2	≤ 0.5	−0.45 ± 0.08	< 0.5	⟨14.3⟩	0.64	15
	12S − 8E	−0.11	4.8	0.5	0.04	−0.50	< 0.5	...	...	0.2	< 0.6					

NOTE.—Rings C9, C10, and C11 are averages at similar but not identical radii.

TABLE 4

OTHER H_2CO OBSERVATIONS

Transition $J_{K_{-1}K_1}$ =	Frequency (GHz)	$\eta_c\eta_{FSS}$	Cloud	T_A^* (K)	V_{LSR} (km s^{-1})	ΔV (km s^{-1})	Resolution (km s^{-1})	T_R[a] (K)	Notes
$3_{12} \rightarrow 2_{12}$ ...	211.211469	0.57	ρ Oph B	1.9(0.13)	3.0	1.8	0.35	3.3	b, c
$3_{12} \rightarrow 2_{11}$ ...	225.697787	0.55	ρ Oph A	2.9(0.6)	2.8	1.4	0.33	5.3	d
	225.697787	0.55	R CrA	2.3(1.1)	4.3	0.5	0.33	4.2	e
$4_{14} \rightarrow 3_{13}$ ...	281.526949	0.49	ρ Oph A	1.4(1.0)	3.0	1.5	0.27	2.9	d
	281.526949	0.49	R CrA	...(1.0)	...	...	1.06	...	e

[a] $T_R = T_A^*/\eta_c\eta_{FSS}$.

[b] The position for ρ Oph B [$\alpha(1950) = 16^h24^m13^s$, $\delta(1950) = -24°19'49''$] was observed before the entire region was mapped and is not exactly at the peak of either 2 cm or 2 mm H_2CO emission.

[c] This line profile appears to be self-absorbed.

[d] The ρ Oph A core position is $\alpha(1950) = 16^h23^m25^s$, $\delta(1950) = -24°15'49''$.

[e] The R CrA core position is $\alpha(1950) = 18^h58^m32^s$, $\delta(1950) = -37°02'08''$.

Toward the ρ Oph cloud pairs of 2 cm and 2 mm H_2CO line profiles were obtained for 69 positions, while data were obtained toward 45 positions for the more southerly R CrA cloud. For all the positions where both 2 cm and 2 mm H_2CO data are available, the line parameters are presented in Tables 1–3. Toward the ρ Oph cloud a number of additional positions were observed in the 2 mm H_2CO line, but no corresponding 2 cm H_2CO lines were obtained. These observations are included in the map but are not tabulated. All positions are given relative to the central ON position, and positions are grouped according to increasing radial distance increments from the densest part of the cloud core for ρ Oph A (Table 1), ρ Oph B (Table 2), and R CrA (Table 3). Along with the H_2CO data, the last column in each table gives the average kinetic temperature, T_K, based on MWO observations of $J = 1$–0 CO toward ρ Oph (Loren *et al.* 1980) and R CrA (Loren 1979). Toward the R CrA cloud, H_2CO data for some positions were taken from Loren, Evans, and Knapp (1979), while others were reobserved.

Additional observations of three higher frequency (211–282 GHz) H_2CO transitions were made at a few selected positions with the MWO antenna. These observations (Table 4) were made with an uncooled version of the receiver, described by Erickson (1981), during 1979 March and 1981 March. Atmospheric opacity was monitored frequently; it was typically 0.3 at the higher frequencies. The data were obtained in a position-switched mode. Calibration was obtained in the same manner as for the 2 mm data. Performance of the antenna at these frequencies has been determined by L. G. Mundy (1981, private communication) from full beam pattern maps of Jupiter. The efficiency, as defined by Kutner and Ulich (1981), for an extended source was determined to be $\eta_{FSS} = 0.83$. The coupling efficiency (η_c) appropriate to the observed cloud size is given in Table 4. The half-power beamwidth decreases from 1.′3 at the lower end of the frequency range to 1.′1 at the upper end.

III. DENSITY MODELS

The 2 cm and 2 mm H_2CO observations can be compared with radiative transfer models to measure the degree of collisional excitation and thus the cloud density. The 2 cm and 2 mm H_2CO lines were first employed to determine cloud densities in several cold dust clouds by Evans and Kutner (1976). The radiative transfer models used in this paper are based on the work of Wootten, Snell, and Evans (1980) and Snell (1981), who use the H_2CO-He collision rates calculated by Green *et al.* (1978). A fundamental feature of these models is that the 2 cm line will pass from absorption to emission at a sufficiently high density ($\sim 10^6$ cm^{-3}). For a resolved region containing a centrally condensed core, the model predicts that a map of the 2 cm absorption strength will have a ringlike distribution. The current observations (§§ IV*b* and V) show that this occurs. The radiative transfer calculation is simplified by the assumption of a large velocity gradient (LVG) in the cloud. We do not contend that such orderly velocity gradients exist in the clouds. Clearly the difference between LVG models and microturbulent models and various geometries in the LVG models (spherically symmetric versus slab) will affect the photon escape probability, but sample comparisons of these alternate models indicate only modestly different results (White 1977; Wootten, Snell, and Evans 1980; Snell 1981). The effects of varying model assumptions and the resultant errors are discussed by Wootten, Snell, and Evans (1980). While the two H_2CO transitions used sample the same volume space, errors will be introduced into the determination of density and abundance since line-of-sight variations of the kinetic temperature, geometry, and density homogeneity affect the degree of radiative trap-

ping. The absolute errors in the density estimate may amount to a factor of 3–5 (Wootten, Snell, and Evans 1980), while the error in the density at one position relative to another is probably less.

The density and $X(H_2CO)$, the relative abundance of H_2CO relative to H_2 in the form $X(H_2CO)/(dV/dR)$, are determined for each position in the cloud from the pair of 2 cm and 2 mm observations. From the maps of density, determined point by point, the center of ρ Oph A (position of highest density) is determined to be closest to the position 1′S-1′W, and for ρ Oph B[7] it is 5′S-11′E, and for R CrA it is 0′N-0′E.

To determine the form of the density profile as a function of radius, the individual observations in a ring of constant radius were averaged, and then the density was found for this average value of the 2 cm and 2 mm intensity. When there is only an upper limit to the 2 cm H_2CO intensity, it is assumed that the line is in absorption rather than emission to determine a limit on the density and abundance. Tables 1–3 show which positions have been averaged together to define each ring. The last five columns in Tables 1–3 give the average 2 cm H_2CO intensity, the average 2 mm H_2CO intensity, the angular distance to the ring (minutes of arc) from the center of the cloud, the projected radial distance (pc), and average T_R^*(CO) of the ring. The density determined from the averages $\langle T_B$ (2 cm)$\rangle$ and $\langle T_R^*$ (2 mm)$\rangle$ is similar to the density determined from the average of densities determined point by point.

IV. THE ρ OPHIUCHI CLOUD

a) *Overall Structure*

Extensive formation of stars in the ρ Oph cloud is revealed by the 2 μm surveys (e.g., Vrba *et al.* 1975; Elias 1978; Wilking and Lada 1982). Self-absorption dominates the appearance of the CO maps of the region (Encrenaz, Falgarone, and Lucas 1975; Loren *et al.* 1980), and specific peaks of the CO do not accurately locate the dense cores.

Figure 1, the map of the intensity of the 2 mm H_2CO transition, reveals two distinct dense cores; the sharply peaked western core is ρ Oph A, and the eastern core is ρ Oph B. The dense core ρ Oph A lies one beamwidth west of the near-infrared source S1 (Grasdalen, Strom, and Strom 1973) = E25 (Elias 1978).[8] This star is coincident with a radio continuum source, BZ 4 (Brown and Zuckerman 1975), and extended far-infrared emission (Fazio *et al.* 1976; Harvey, Campbell, and Hoffman 1979). The radio flux requires the equivalent of a B3 V star, in agreement with the far-infrared luminosity of 400 $L_\odot$, which requires a B5 V star. S1 is sufficiently evolved that it has created a low-density cavity in the dust distribution around it (Harvey, Campbell, and Hoffman 1979), in agreement with the displacement of the star from the density peak indicated in the H_2CO map. There is no known embedded infrared object at the position of the dense core.

The only objects within the boundaries of the 2 cm H_2CO emission region at ρ Oph B (indicated by cross hatching in Fig. 1) are a cluster of three near-infrared sources (Wilking and Lada 1982), which were previously unresolved and identified as VS 26 (Vrba *et al.* 1975). These sources coincide with a radio continuum source, FG 12 (Falgarone and Gilmore 1981). There has been no far-infrared emission detected in the ρ Oph B region (Fazio *et al.* 1976). Loren and Wootten (1983) have found exceptionally strong DCO^+ emission throughout the ρ Oph B region; in comparison, the DCO^+ emission from the ρ Oph A core is only one-fourth as strong.

The stars within the vicinity of ρ Oph A and B may have formed within dense cores which are no longer present or within portions of the currently observable dense cores. The present dense cores may be the site of future formation of massive stars. In addition to the ρ Oph A and ρ Oph B cores there is a plateau of weak 2 mm H_2CO emission that extends to the south and includes the infrared source E29 (Elias 1978). The region where Lada and Wilking (1980) find the most prominent ^{13}CO self-absorption, indicated in Figure 1, does not coincide with either ρ Oph A or ρ Oph B but lies 4′S-5′W of ρ Oph B. The weakness of the 2 mm H_2CO line at this position indicates that no distinct dense core exists at this position, but that there is only a long path length of moderate to low density ($< 10^4$ cm^{-3}) gas. A map of $J = 1$–0 $C^{18}O$ toward ρ Oph (Wilking and Lada 1982) shows a column density peak near the position of ^{13}CO self-absorption and a second peak near ρ Oph A. The $C^{18}O$ map shows no peak at ρ Oph B, indicating that a much shorter path length of low-density gas exists there.

b) *The ρ Ophiuchi A Core*

In Figure 2 the distribution of intensity of the 2 cm H_2CO transition is shown. While strong absorption is seen at many positions, in the vicinity of ρ Oph A there are either no detectable 2 cm lines (emission or absorption) or only weak absorption. This cavity in the 2 cm H_2CO distribution corresponds to the region of strongest 2 mm H_2CO intensity, confirming that the absorption of the 2 cm transition is disappearing not as a result

[7]The cores of ρ Oph A and R CrA are well defined since the strongest 2 mm H_2CO emission is sharply peaked, indicating a compact source. The position of the core of ρ Oph B is not as well determined since the 2 mm H_2CO suffers self-absorption (Loren *et al.* 1980), and the peak of the optically thin DCO^+ emission lies to the NE of the strongest 2 cm H_2CO emission (Loren and Wootten 1983).

[8]Infrared sources labeled S are from the 2 μm survey of Grasdalen, Strom, and Strom (1973); those labeled E, from Elias (1978); and those labeled VS, from Vrba *et al.* (1975).

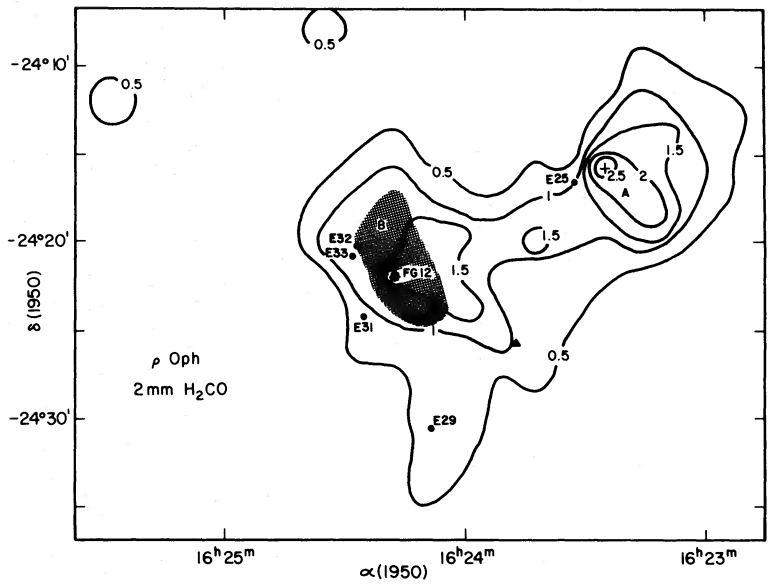

FIG. 1.—The distribution of intensity expressed as T_R^* of the $J_{K_{-1}K_1} = 2_{12}-1_{11}$ transition of H_2CO in the ρ Oph molecular cloud. The reference position is indicated by a cross which lies near the ρ Oph A core. The ρ Oph B core lies to the east, and the region of 2 cm H_2CO emission is shaded. The positions of a few of the important infrared sources near ρ Oph B are plotted as filled circles (Elias 1978), the radio continuum source FG 12 is indicated by a square (Falgarone and Gilmore 1981), and the triangle represents a position of ^{13}CO self-absorption (Lada and Wilking 1980).

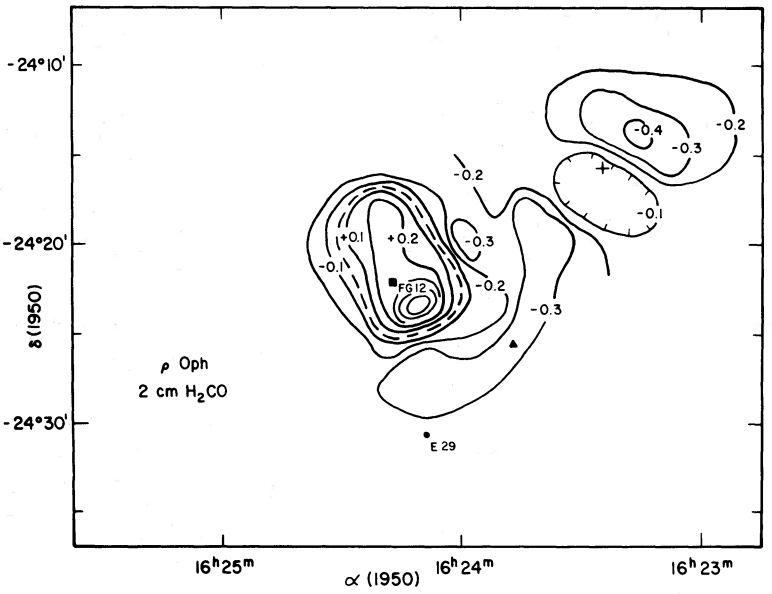

FIG. 2.—The distribution of intensity expressed as T_B of the $J_{K_{-1}K_1} = 2_{12}-2_{11}$ transition of H_2CO toward ρ Oph. The symbols are as in Fig. 1.

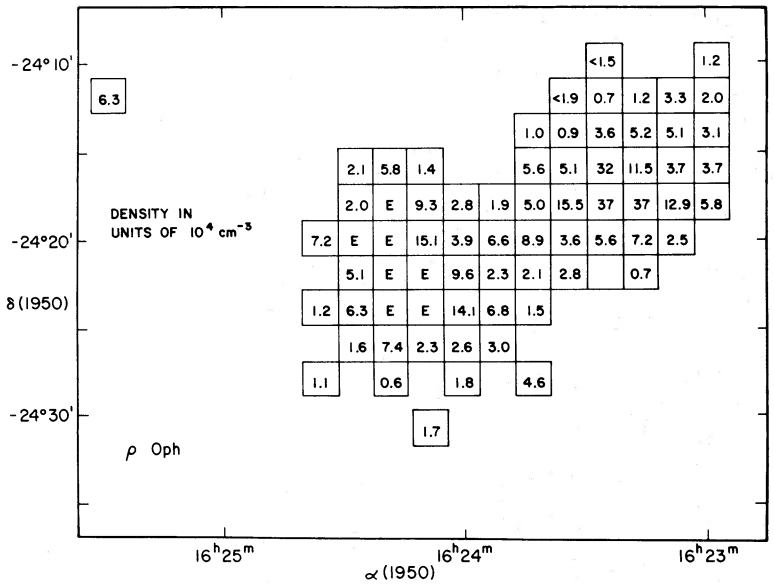

FIG. 3.—The distribution of density toward the ρ Oph molecular cloud. The squares with an E indicate positions where the 2 cm H_2CO was detected in emission and the density is greater than 10^6 cm^{-3}.

of low density but rather as a result of high density and the approach to thermalization of the level population. To the NW and SE of the ρ Oph A core, the 2 cm H_2CO absorption-line strength increases, while the 2 mm H_2CO emission intensity decreases, a result of decreasing cloud density in these regions.

The density and $X(H_2CO)/(dV/dR)$ are derived for each observed position assuming that each point is independent of any other point in the cloud. As a result, the abundance $X(H_2CO)/(dV/dR)$ is essentially a free parameter in fitting the models. We find an inverse correlation between density and $X(H_2CO)/(dV/dR)$ similar to that previously noted by Wootten *et al.* (1978). We attempted to construct models in which $X(H_2CO)/(dV/dR)$ was constant throughout the cloud, but this proved to be too severe a constraint since the radial variation of the 2 cm and 2 mm H_2CO intensities could not be matched. The spatial distribution of density we have calculated is plotted in Figure 3. This map clearly shows that very steep density gradients are present at each of the two cores in this cloud. In ρ Oph A the density drops from 3×10^5 cm^{-3} at the core to 1×10^4 cm^{-3} at a position 2.'8, or 0.12 pc, to the NE. Likewise, the density at ρ Oph B drops from over 10^6 cm^{-3} to 1×10^4 cm^{-3} within 0.2 to 0.3 pc.

Toward ρ Oph A five radial distances are well sampled, and some partial data exist at larger radii. Using a distance of 160 pc (Whittet 1974), the innermost radial ring lies at 0.06 pc and the outermost at 0.37 pc from the cloud center. The averages $\langle T_R^*$ (2 mm)$\rangle$ and $\langle T_B$ (2 cm)$\rangle$ are plotted in Figure 4 against the projected radial distance (R) from the cloud center, where the error bars represent only the internal scatter. The spatial distribution of density (Fig. 3) is somewhat nonspherical, but averaging in rings suppresses this asymmetry. The radial density profile derived from the averaged observations from Figure 4 is plotted in Figure 5. The density decreases with increasing projected radial distance in a manner that is well fitted by a power law [$\rho(R) \propto R^\alpha$, where $\alpha = -3/2$ to -2]. The density drops by about two orders of magnitude in a distance of 1 pc. Such a

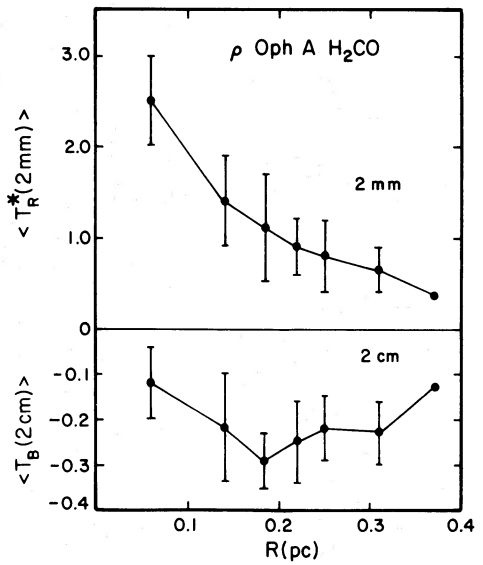

FIG. 4.—The radial variation of the average H_2CO T_R^* (2 mm) and T_B (2 cm) toward the ρ Oph A dense core.

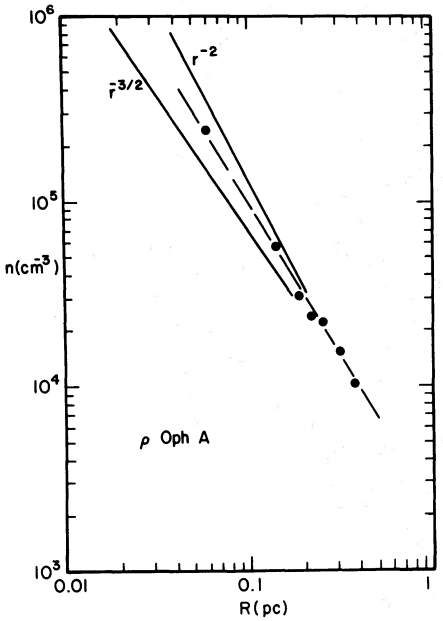

FIG. 5.—The density of the ρ Oph A core vs. projected radial distance.

sharp density gradient bears a striking resemblance to Larson's (1969, 1972) models of the collapse of a gas cloud to form a protostar. The core size is defined as the radius at which the density has dropped to half the maximum observed value. From Figure 5 we find a core size of 0.09 pc for a density of $\gtrsim 3 \times 10^5$ cm^{-3}, resulting in a core mass of at least 50 $M_\odot$ for ρ Oph A. It should be noted that if such a compact dense core existed in a much more distant cloud, it would be difficult to resolve because of beam dilution. There is no evidence of a flattening of the density profile at large R that might be due to the presence of a uniform envelope with a density over 10^4 cm^{-3}.

c) *The ρ Ophiuchi B Core*

In the direction of the ρ Oph B core the density becomes high enough to drive the 2 cm H_2CO transition into emission over a $8' \times 4'$ region (Fig. 2). In contrast, the 2 cm emission regions in OMC-1 (Evans *et al.* 1975) and OMC-2 (Kutner, Evans, and Tucker 1976) are essentially unresolved. Since these clouds are more distant, the sizes of the emission regions may be similar. The T_R^*(CO) ~ 30 K observed at ρ Oph B is much colder than that in OMC-1 [T_R^*(CO) ~ 90 K] or OMC-2 [T_R^*(CO) ~ 60 K]. The peak T_R^*(CO) seen toward ρ Oph B may occur in a background cloud since very strong DCO^+ emission coincides with the 2 cm H_2CO emission region (Loren and Wootten 1983). The DCO^+ molecule has an enhanced abundance only in rather cold dense clouds (Wootten, Loren, and Snell 1982). The lower density part of this cold region is probably responsible for the widespread absorption that occurs in the CO and ^{13}CO line profiles.

The H_2CO observations toward ρ Oph B extend to even greater distances from the core than in ρ Oph A. The radial variation of the averages $\langle T_R^*$ (2 mm)$\rangle$ and $\langle T_B$ (2 cm)$\rangle$ are shown in Figure 6. In contrast to ρ Oph A, the 2 mm line intensity is not sharply peaked spatially. This can be the result of self-absorption of the 2 mm line since the line profile appears double peaked, while optically thin lines are singly peaked at a velocity near the dip of the 2 mm line (Loren *et al.* 1980). The occurrence of 2 mm H_2CO self-absorption where the 2 cm H_2CO goes into emission precludes finding definitive density models, although the densities must be high for 2 cm emission to occur. In the region where the 2 cm line is in emission, the typical 2 mm line strength is $T_R^* = 1.8$ K. In any models in which the 2 cm line goes into emission, a lower kinetic temperature will produce weaker 2 mm lines. From the H_2CO models of Snell (1981) one finds, for $T_K = 30$ K (as indicated by the CO) and densities of less than 10^6 cm^{-3}, the 2 cm H_2CO line goes into emission only when the corresponding 2 mm line has intensities in excess of 8 K, much greater than observed. This problem is only partially alleviated for the reduced values of T_K required by the strong DCO^+. Figure 7 shows H_2CO models at $T_K = 15$ K. The cross-hatching defines the region where the 2 cm line is in absorption. Trying to model the 2 mm and 2 cm strength in the core of ρ Oph B, it can be seen that the curve of 2 mm line strength of 1.8 K does not intersect the curve for +0.25 K emission strength of the 2 cm transition in

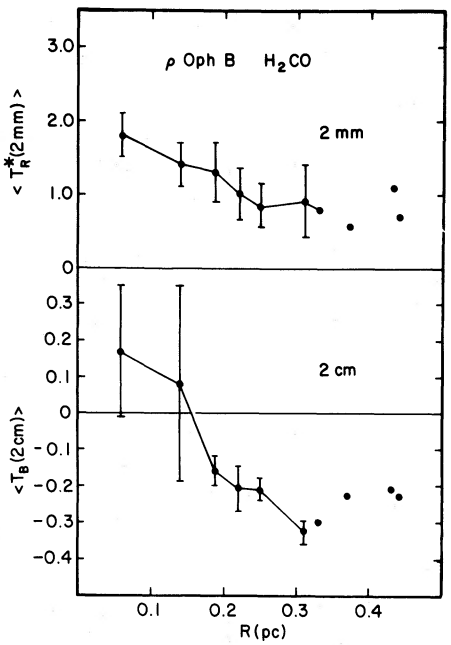

FIG. 6.—The radial variation of the average H_2CO T_R^* (2 mm) and T_B (2 cm) toward the ρ Oph B dense core.

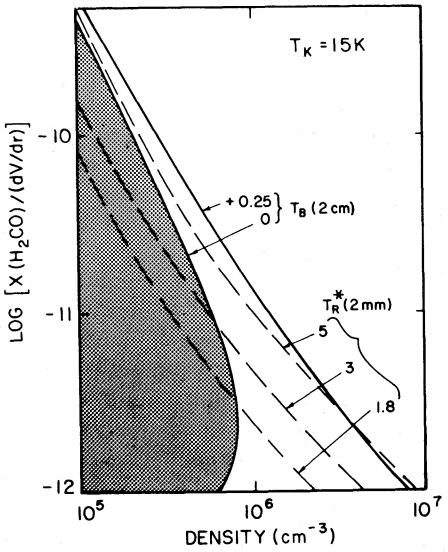

FIG. 7.—LVG statistical equilibrium calculations of H_2CO for a kinetic temperature of 15 K. Contours of 2 cm H_2CO intensity are shown as solid lines. The shaded area corresponds to 2 cm absorption; 2 cm emission lies to the right of this region. Contours of 2 mm H_2CO intensity are shown as dashed lines.

the range of density from 10^5–10^7 cm^{-3}. Since the curves are roughly parallel, there is no acceptable solution unless the 2 mm line intensity toward ρ Oph B is considerably reduced by self-absorption. For instance, a possible solution at a density of $10^{6.5}$ cm^{-3} would occur if the undiminished intensity of the 2 mm line were 5 K. Even if the 2 mm line were not affected by self-absorption, the density would not be well determined since the 2 mm and the 2 cm line strength curves are very nearly parallel when the 2 cm line goes into emission. Observations of additional H_2CO transitions are needed to adequately model the density of the region of 2 cm emission, but minimum densities of 10^6 cm^{-3} are required. Independent estimates of the density have been obtained from observations of the $J = 1$–0 and $J = 3$–2 lines of HCO^+ and $H^{13}CO^+$ (Loren *et al.* 1983). These observations require a density of 3×10^5 cm^{-3} toward ρ Oph A and $\sim 8 \times 10^5$ cm^{-3} toward a position near ρ Oph B, both in agreement with the density derived from H_2CO.

In the envelope of the ρ Oph B core the density versus R plot (Fig. 8) is a power law of R^{-2} similar to that found for the ρ Oph A core. If the densities of the inner core are in excess of 10^6 cm^{-3}, then a steeper density gradient occurs within this region. A steeper density gradient might be due to shock compression, and a possible origin for such a shock is discussed by Loren and Wootten (1983). The density of the core drops by two orders of magnitude in a distance of 0.4 pc. From Figure 8 a core size of 0.08 pc is found with a peak density $\gtrsim 10^6$ cm^{-3}, which results in a core mass of 110 $M_\odot$.

d) H_2CO *Abundances*

Figure 9 all of the ρ Oph data are combined in a plot of the abundance parameter $X(H_2CO)/(dV/dR)$ versus density. The sharply defined straight line in this log-log plot indicates that the H_2CO abundance decreases in the high-density core, a phenomenon which occurs from cloud to cloud (Wootten *et al.* 1978; Wootten, Snell, and Evans 1980) or within a single cloud (Loren, Evans, and Knapp 1979). Ion-molecule chemistry predicts some decrease of $X(H_2CO)$ with density (e.g., Wootten, Snell, and Evans 1980), but not as steep as that observed. Other possible molecular depletion processes include ultraviolet (UV) photodissociation by embedded stars (Bernes and Sandqvist 1977) and accretion of gas phase molecules onto dust grains with increasing density. Both of these processes will be discussed below, and a discussion of how the basic assumptions in the radiative transfer models might alter the $X(H_2CO)/(dV/dR)$ versus density relation will be deferred until § VI*a*.

A possible source of UV photodissociation has been identified (at a position $\sim 2'$E of the ρ Oph A core) as the embedded radio continuum source BZ 4 (Brown and Zuckerman 1975), with associated carbon recombination line emission (Brown *et al.* 1974) and far-infrared continuum emission (Harvey, Campbell, and Hoffman

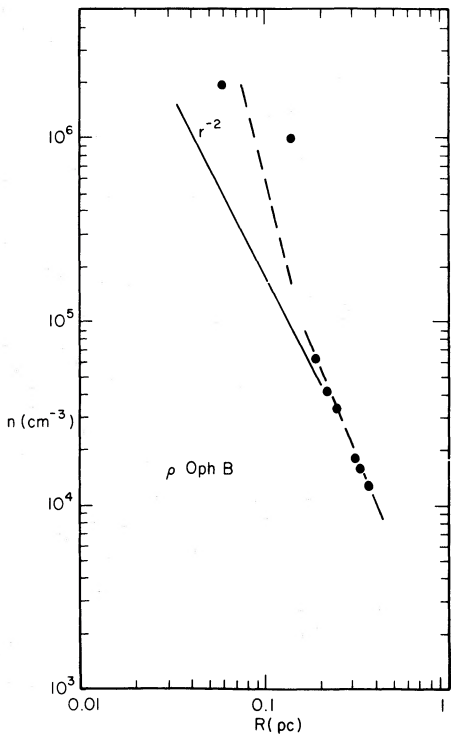

FIG. 8.—The density of the ρ Oph B core vs. projected radial distance. The region surrounding E29 (zone B10) appears to be a separate part of the cloud on the basis of its V_{LSR}, and points in this part of the cloud are excluded from this plot.

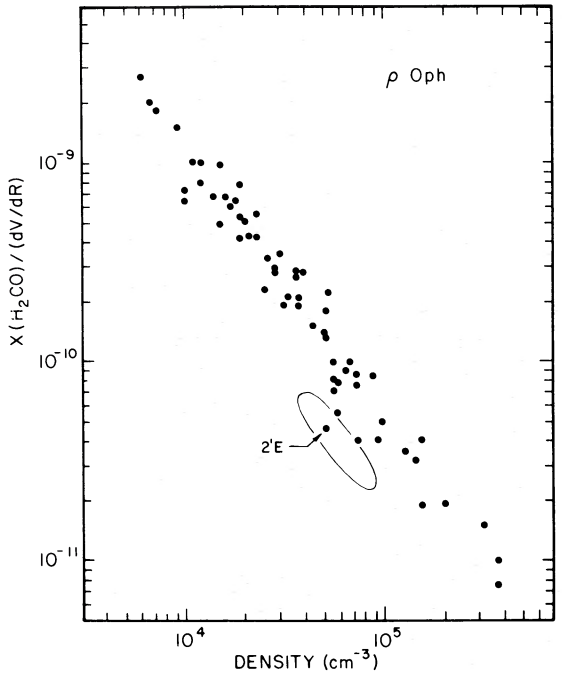

FIG. 9.—The abundance parameter of H_2CO, $X(H_2CO)/(dV/dR)$, vs. density in the ρ Oph cloud.

1979). For the density observed toward BZ 4 (the point labeled 2′E in Fig. 9), the value of $X(H_2CO)/(dV/dR)$ lies considerably below the linear trend defined by the other points in the cloud. To ascertain the significance of this deviation, an error ellipse has been plotted about this point using the 1 σ errors of the 2 cm and 2 mm observations. The errors are largest in the direction parallel to the average $X(H_2CO)/(dV/dR)$-density relation but much smaller in a perpendicular direction. Therefore, we conclude the displacement is significant and requires a lower $X(H_2CO)$, which we attribute to local UV photodissociation of H_2CO by BZ 4. Photodissociation fails to explain the overall decrease in H_2CO abundance with increasing density since the UV photons should be shielded more effectively in the dense regions, and $X(H_2CO)$ should increase with density. UV photodissociation by ambient intercloud photons should be important in the very low density regions of clouds. As a result, at some low density the abundance of H_2CO should again begin to decrease.

Wootten, Snell, and Evans (1980) have proposed that in very dense regions heavy molecules condense onto grains, resulting in their apparent depletion in the gas phase within the cloud core. For several reasons, this is especially appealing for the observations of the ρ Oph cores. Anomalously large interstellar extinction has long been known to characterize the dust in the ρ Oph complex. The polarimetry of Carrasco, Strom, and Strom (1973) and the wide-band photometry of Vrba *et al.* (1975) demonstrate that in dense regions of the cloud, grain sizes are 1.5–2 times the size of those in peripheral regions. Increased grain sizes are also found in the R CrA cloud (Vrba, Coyne, and Tapia 1981). Multiband photometry (Harris, Woolf, and Rieke 1978) of the 3.1 μm absorption band of interstellar ice showed that in the densest regions of ρ Oph, ice molecules are condensed onto grains. In fact, the strongest ice absorption in their survey was observed toward VS 26, the object(s) nearest the very cold, very dense ρ Oph B core. The presence of H_2CO in grain mantles is confirmed by the detection of a 3.5 μm emission feature (Blades and Whittet 1980) which in high spectral resolution observations matches the detailed shape of the laboratory spectra of a mixture of monomer and dimer H_2CO (Baas *et al.* 1983). The accretion of gas phase molecules onto grains with increasing cloud densities is supported by the absence of the 3.1 μm ice feature in the infrared spectra of the galactic center (Soifer, Russell and Merrill 1976; Willner *et al.* 1979). The large extinction to the galactic center comes from low-density material along the line of sight, not from cold, high-density molecular clouds.

While uncertainties of the H_2CO models (§ VI*a*) may alter the slope of the $X(H_2CO)/(dV/dR)$ versus density relation, the overall trend remains. The accretion of gas phase molecules onto grains provides a natural and compelling explanation for the decline in the gas phase abundance of H_2CO and other molecules while simultaneously accounting for the increase of grain size with increasing extinction and the existence of observable ice mantles on grains in only the densest regions of molecular clouds.

e) *Velocity Pattern*

One might hope to distinguish various regions of the cloud on the basis of differences in V_{LSR}, velocity with respect to the local standard of rest. The variation in V_{LSR} of the peak of the 2 mm H_2CO profile is shown in Figure 10. It is known that the peak of the 2 mm H_2CO line is shifted to slightly lower velocity in the vicinity of ρ Oph B by self-absorption (Loren *et al.* 1980). This may also occur near ρ Oph A, where the line peak occurs slightly below 3 km s^{-1}. At two isolated positions to the NE, peak emission occurs at a velocity of 3.7 km s^{-1}, near that of the optically thin lines in ρ Oph B (3.6 km s^{-1}).

The only region of distinctly different velocity is that surrounding E29, where the peak H_2CO velocities lie between 4.5 and 4.9 km s^{-1}. This region may define a separate clump which may contribute to some of the secondary emission seen in CO and ^{13}CO (Lada and Wilking 1980). The maximum densities that occur near E29 are low for the ρ Oph cloud (a few times 10^4 cm^{-3}), similar to the densities encountered in dust clouds like L134N or L1529.

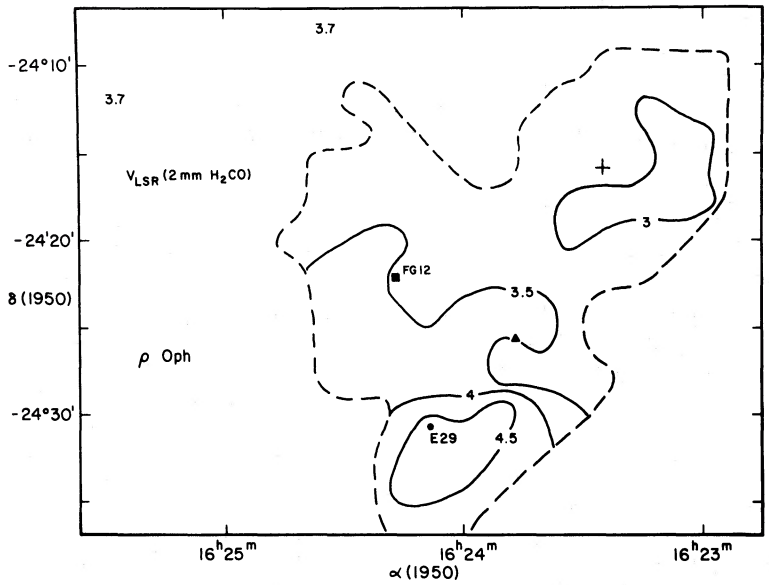

FIG. 10.—The V_{LSR} of the 2 mm H_2CO toward the ρ Oph cloud. The symbols are as in Fig. 1.

f) Comparison of Temperature and Density Structure in ρ Ophiuchi

In most molecular clouds the temperature and density peaks appear to be coincident. This coincidence could be due to lack of adequate spatial resolution, or it could be real, resulting from a newly formed high-luminosity star in intimate association with dense material from which it formed. The high spatial resolution afforded in the ρ Oph cloud allows us to make a detailed comparison of the spatial separation of temperature and density peaks. In Figure 11 the $J=1$–0 CO map (Loren *et al.* 1980) is compared with the density contours of 5×10^4 cm^{-3} and 2×10^5 cm^{-3} based on the density map in Figure 3. The strongest CO is not coincident with the high density peak at ρ Oph A but occurs in a ridge of $T_A^*(CO)=40$ K along the SW side of the dense core. Toward the ρ Oph B high-density core the CO shows only a modest enhancement. The CO may not peak sharply at the positions of highest density due to the self-absorption or because of their low temperature. DCO^+ is a molecule whose abundance is sensitive to temperature. In Figure 11 the shaded area corresponds to regions of $J=2$–1 DCO^+ emission which exceed $T_A^*=1.2$ K (discussed more extensively in Loren and Wootten 1983). Strong DCO^+ emission, resulting from high density and enhanced abundance, occurs only in cold dense clouds (Wootten, Loren, and Snell 1982). These strong DCO^+ emission regions in ρ Oph are cold and anticorrelate with the regions of strong CO emission. Further evidence for the cold dust grains toward ρ Oph B is found in very strong infrared absorption due to ice at 3.1 μm toward the stars E32, E33, and VS 26 (Harris, Woolf, and Rieke 1978). The strongest ice absorption occurs toward VS 26, which lies closest to the center of the DCO^+ emission region. The 3.1 μm absorption feature, produced by ice mantles on grains, is likely to originate in a cold region since molecules which condense on grains cannot subsequently evaporate off the grain at temperatures below 17 K (Watson and Salpeter 1972; Aannestad 1973). Therefore, not only the gas but also the dust within ρ Oph B is cold.

The most prominent CO peak [$T_A^*(CO)=50$ K] coincides with the infrared source E16. This high temperature occurs in a relatively low density portion of the cloud and is another example of the temperature and density peaks not coinciding on the small spatial scale of the ρ Oph cloud observations.

V. THE R CORONAE AUSTRALIS CLOUD

A dark cloud in CrA is a region of active star formation (Knacke *et al.* 1973; Vrba, Strom, and Strom 1976*a*) including Herbig-Haro objects (Strom, Strom, and Grasdalen 1974), 2 μm sources, and the young Ae star R CrA (Herbig 1960), which illuminates the NGC 6729 nebula. The distance to the cloud is 129 pc (Marraco and Rydgren 1981). Brown and Zuckerman (1975) have detected a radio continuum source at a position within 20″ of R CrA which has no optical or 2 μm counterpart. They suggest the radio flux arises in a compact H II region excited by a B3 or earlier type star embedded in the dense core. The far-infrared (70–200 μm) emission detected by de Muizon *et al.* (1980) is far less than a B3 star would produce. The measured luminosity of $L_{IR}=140\ L_\odot$ would correspond to only a B7 star, in reasonable agreement with the spectral type of R CrA (Ae, Knacke *et al.* 1973). A possible explanation of the radio

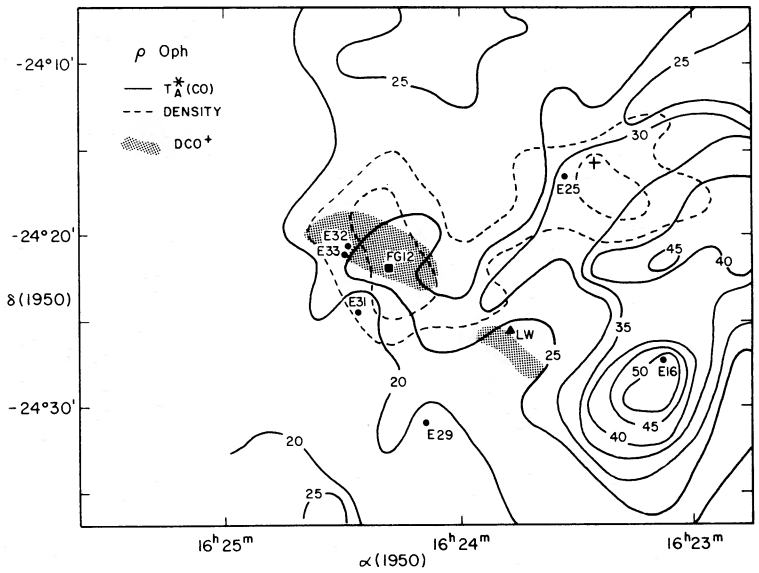

FIG. 11.—Comparison of temperature and density distributions in ρ Oph. Solid contours are T_A^*(CO) for the $J = 1-0$ line. The dashed contours correspond to densities of 5×10^4 and 2×10^5 cm^{-3} as determined from the H_2CO observations. The crosshatched regions correspond to DCO^+ $J = 2-1$ emission which exceeds 1.2 K. The reference position (ON) is indicated by a cross, and infrared sources by filled circles. The continuum source FG 12 (Falgarone and Gilmore 1981) is indicated by a square, and the ^{13}CO self-absorption position (Lada and Wilking 1980) by a triangle.

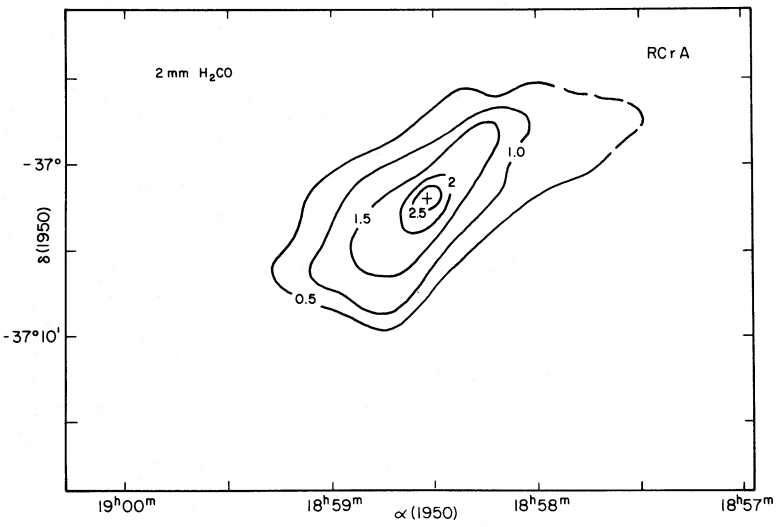

FIG. 12.—The distribution of intensity expressed as T_R^* of the $J_{K_{-1}K_1} = 2_{12}-1_{11}$ transition of H_2CO in the R CrA molecular cloud. The position of R CrA is indicated by a cross.

continuum emission observed by Brown and Zuckerman is that it arises in a collisionally ionized stellar wind, which could also account for the enhanced broadening of the CO lines at R CrA (Loren 1979).

The visual reddening toward R CrA requires only a few magnitudes of extinction toward the star, far less than the amount expected to the center of a dense core. The only star identified toward the dense core, R CrA, lies closer to the surface than to the center of the cloud. The lack of any excess far-infrared luminosity indicates that no stars more massive than A0 are embedded within the dense core. The potential exists for the formation of massive stars within the CrA dense core, but so far this has not occurred.

Figure 12 shows that the distribution of strongest 2 mm H_2CO emission in CrA is elongated from SE to NW, an alignment which is in agreement with the direction of optical polarization (and inferred magnetic

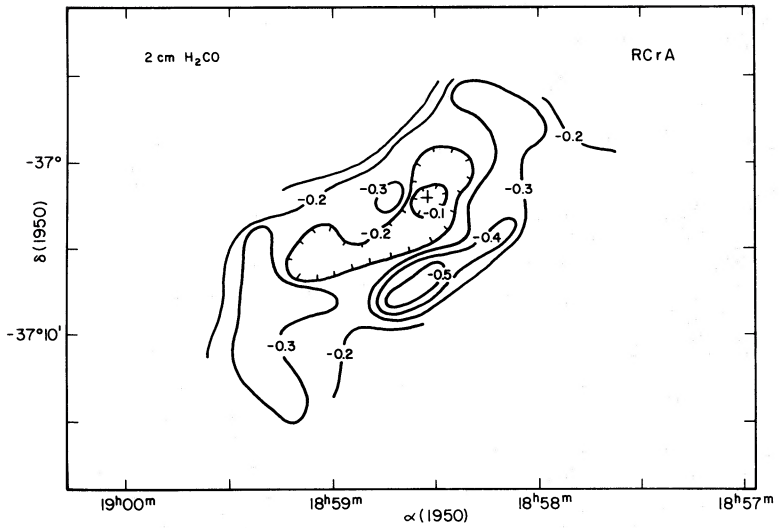

FIG. 13.—The distribution of intensity expressed as T_B of the $J_{K_{-1}K_1} = 2_{12}-2_{11}$ transition of H_2CO toward R CrA

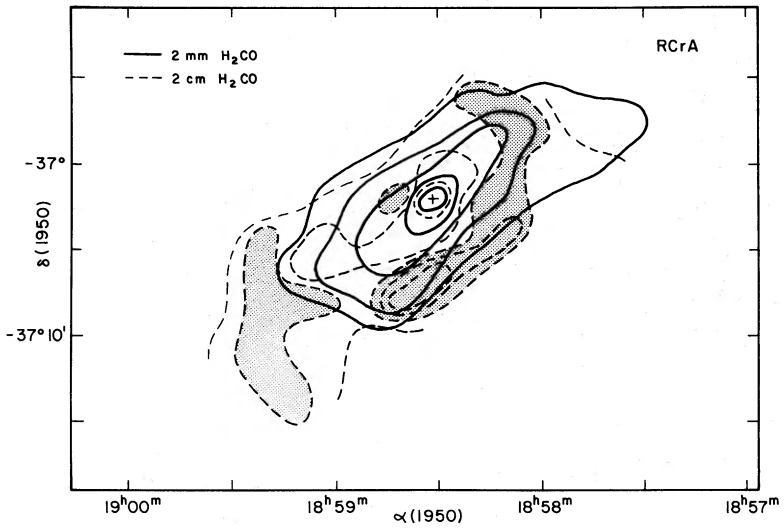

FIG. 14.—A comparison of the 2 cm and 2 mm H_2CO toward R CrA showing the anticorrelation of 2 cm absorption strength and 2 mm emission strength in the dense core. The strongest 2 cm absorption is shown by shading.

field orientation) determined by Vrba, Strom, and Strom (1976*b*). The peak 2 mm H_2CO emission lies at the position of the foreground pre–main-sequence star R CrA. In Figure 13, the distribution of the 2 cm H_2CO absorption strength toward R CrA illustrates the weakening of the absorption strength that occurs at high densities. A "hole" of weak 2 cm absorption coincides with the peak of the 2 mm H_2CO distribution. This is more clearly shown in Figure 14, in which the 2 cm and 2 mm maps are superposed. The strongest 2 cm absorption occurs in a (shaded) ring around the dense core.

The densities found from the H_2CO measurements reveal (Fig. 15) that the density is highest toward the position of R CrA and decreases rapidly away from this core. This decrease in density is sharpest in the direction perpendicular to the elongation of the dust cloud. As in the ρ Oph cloud, densities have been determined from the intensities averaged at positions equidistant from the cloud core (Table 3). The average radial density variation is shown in Figure 16. The best overall fit is a power law of roughly $R^{-3/2}$. The density drops by two orders of magnitude over a distance of 0.8 pc along the major axis and a distance of 0.5 pc along the minor axis. For a core size of 0.06 pc and a central density of 4×10^5 cm^{-3}, the core mass is 19 $M_\odot$.

Just as in the ρ Oph cloud, $X(H_2CO)/(dV/dR)$ decreases sharply with increasing density (Fig. 17). This apparent decrease of $X(H_2CO)$ might be due, instead, to

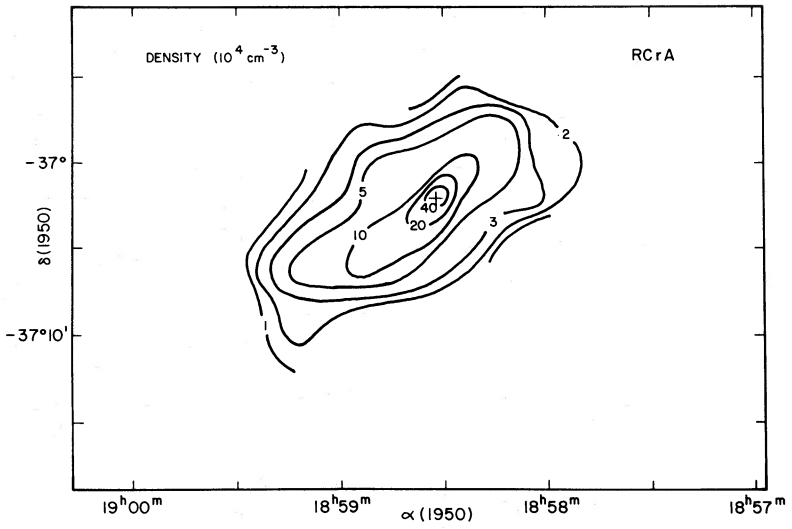

FIG. 15.—The distribution of density toward the R CrA cloud

variation of the density structure along the line of sight. We can test the hypothesis that a unique $X(H_2CO)$ applies throughout the cloud with specific models. Fixing $X(H_2CO)$ at a constant value required by the observations in the low-density envelope of the R CrA cloud, a model was constructed incorporating both density and temperature gradients. The best fits for the integrated line intensities at the core are achieved for density gradients between $r^{-3/2}$ to r^{-2} power laws. The cloud core intensities can be matched to the models, but at any position away from the core both the 2 cm and 2 mm model line intensities decrease much too rapidly in comparison with the observations. The disagreement becomes an order of magnitude by the first radial ring (C1). Relaxing the constant abundance constraint, a model has been calculated for the R CrA cloud which incorporates a radial density gradient ($n \propto r^{-3/2}$). The model has a low-abundance core [$X(H_2CO) = 5 \times 10^{-11}$ for densities $n > 10^6$ cm^{-3}], a high-abundance envelope [$X(H_2CO) = 1.5 \times 10^{-9}$ for $n < 10^4$ cm^{-3}], and a transition region where $X(H_2CO)$ follows the relation in Figure 17 for a density range of $10^4 < n < 10^6$ cm^{-3} and $dV/dR = 9.5$ km s^{-1} pc^{-1}. This model successfully reproduces the radial falloff of integrated intensity (within a factor of 2) for both the 2 cm and 2 mm lines as well as the line intensities and widths at the center position. Adjustment of the input parameters could provide a better fit to the data but seems unwarranted given the other uncertainties. This model does demonstrate the consistency of the simpler modeling procedure. A model incorporating density and abundance variations can successfully fit the data in contrast to the uniform abundance model in which the predicted variation in integrated intensity is too steep to be consistent with the observations.

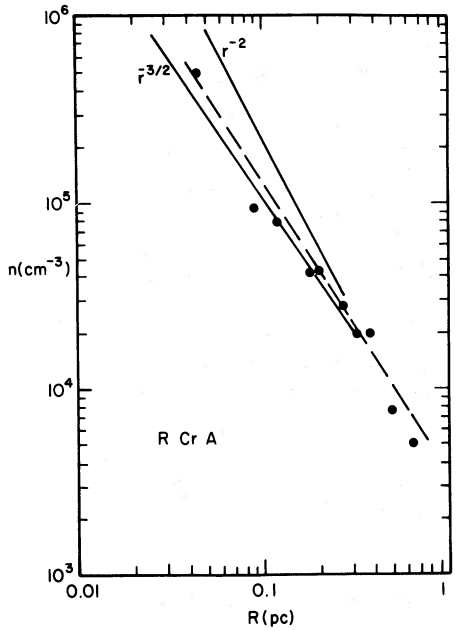

FIG. 16.—The density of the R CrA core vs. projected radial distance. For the purpose of this log-log plot the density of the central zone is plotted at a projected radial distance of 0.045 pc corresponding to half the beam size. Since zones C5, C6, and C7 are at roughly the same distance, they are combined into a single point.

We need to examine alternative causes of the apparent $X(H_2CO)$ decrease. Detection of $J = 2$–1 DCO^+ emission of moderate intensity (0.5 K), typical of many cold dense clouds, signals that the dense core is cold with a low electron density (Wootten, Loren, and Snell 1982). One possible geometry locates R CrA itself along the line of sight to the core, with both the continuum

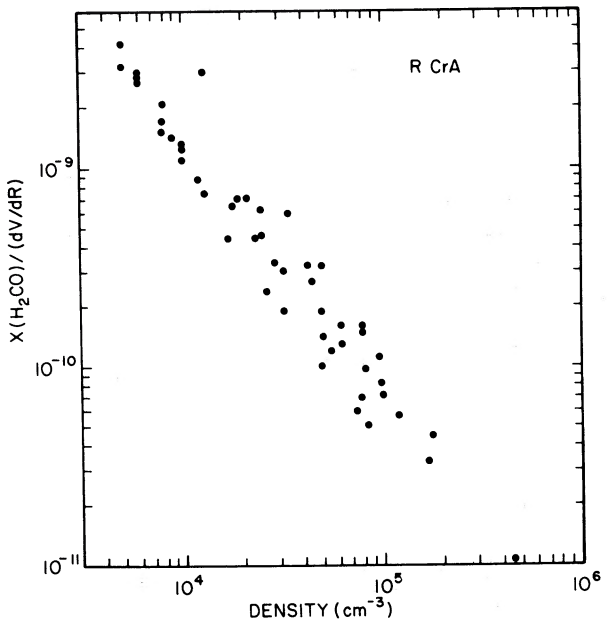

FIG. 17.—The abundance parameter $X(H_2CO)/(dV/dR)$ vs. density in the R CrA cloud.

source and CO hot spot appearing as surface manifestations of an interaction between the star and the cloud core. This geometry is unfavorable for detecting the role of photodissociation in depression of the H_2CO abundance near the core. As has been hypothesized for ρ Oph, we suggest that a local process such as photodissociation plays only a minor causative role. Like the ρ Oph cloud the grain size increases with extinction through the R CrA cloud (Vrba, Coyne, and Tapia 1981). At high densities and, consequently, large extinctions, the radio observations require a declining gas phase abundance of H_2CO. Our conclusion is that at least 90% of the H_2CO molecules which are present in the gas phase at densities below 10^4 cm^{-3} can no longer be detected from regions of high density (10^6 cm^{-3}). As in the ρ Oph cloud a single physical mechanism, condensation of material onto grains in cold dense regions, can effectively explain a variety of results.

VI. DISCUSSION

a) Accuracy of Model Interpretation

To assess the accuracy of obtaining the radial variation of density by comparing the H_2CO observations with radiative transfer models, some of the underlying assumptions which go into the models should be reexamined. Wootten, Snell, and Evans (1980) have extensively discussed a variety of sources of error in the LVG radiative transfer models and find that one of the most important is the assumption of density homogeneity. In the models in this paper the density and H_2CO abundance at each position in the cloud have been determined using a uniform density and abundance along that line of sight. This is unlikely to be true since the maps of both the ρ Oph and R CrA cores show that steep density gradients are present. Even if density and $X(H_2CO)$ vary smoothly, the line of sight toward the cloud core will sample the full range of variation of physical conditions. Part of the low-density, high H_2CO abundance envelope will be in front of the dense core, and its effect on the strong 2 mm core emission will be minimal, but the effect on weak 2 cm core emission will be greater. In a spherically symmetric cloud, the line of sight toward the core will have a shorter path length through the low-density envelope than any line of sight that is more tangential to the envelope. Even so, this high H_2CO abundance envelope must produce some 2 cm absorption. Since only weak absorption or emission, in the 2 cm lines, is observed toward the cloud cores, any expected envelope absorption must be balanced by even stronger 2 cm emission from the core. Stronger 2 cm emission would require higher core densities and therefore a steeper density gradient than calculated from the uniform abundance case. With a sharp radial density drop-off, the low-density envelope may actually provide relatively little contribution to the core emission of either H_2CO line. The conclusion that there are steep density gradients in the cloud cores is not changed; only the slope is slightly increased.

Knowing that sharp density and abundance gradients exist in the clouds, radiative transfer models which specify these variations should predict the proper variation of the intensities of the two H_2CO lines across the face of the cloud. This added complexity may be too great for a LVG radiative transport code to handle realistically. For example, the imposed velocity gradient in the code will produce line width variations across the face of the cloud which are much greater than allowed by the observations. Comparisons can be restricted to integrated intensities, but a LVG code still may not adequately predict strengths for the optically thick 2 mm lines. Even so, in the last section, we found that the LVG models did fit the data quite well.

A second problem for any radiative transfer code is that the apparent $X(H_2CO)$ decrease with density (Figs. 9 and 17) may arise either from a real decrease of $X(H_2CO)$ or from density inhomogeneities which preferentially affect one line relative to the other. In fact our observations of the structure of the ρ Oph cloud provide clear evidence for the presence of density inhomogeneities since at least two nearby condensed cores are present. Further clumping within the beam can substantially reduce the 2 mm line strength but will have less effect on the 2 cm line. If a uniform abundance model is used to interpret such a clumpy region, the $X(H_2CO)$ will be underestimated for a given density. Clumping can account for some of the apparent decrease of

$X(H_2CO)$ with density, but it seems unlikely that the entire effect is due to clumping. The observed apparent $X(H_2CO)$ decrease spans more than two orders of magnitude with relatively little scatter. Unless the filling factor of a random ensemble of clumps varied smoothly and slowly as a function of density, one would expect to observe a great deal more scatter in the $X(H_2CO)$ versus density relationship as a greater or lesser number of clumps are included in the beam. Some limits can be placed on the degree of clumping by the H_2CO observations. If the number of clumps m, at radiation temperature T_c, fill a fraction f_c of the beam area, a line of intensity mf_cT_c will be produced. Any of these factors may be varied to match the observed line intensity. If the maximum T_c is the kinetic temperature (derived from CO [Loren 1979; Loren *et al.* 1980] or dust [de Muizon *et al.* 1980]), the observed strength of the 2 mm lines limits clumping to $mf_c \geq 0.1$ (for R CrA) and $mf_c \geq 0.05$ (for ρ Oph). Because the 2 cm line is optically thin and observed in absorption against the 3 K cosmic background radiation, a further constraint on mf_c can be obtained. Thermalization of the clumps is ruled out by the weakness of the 2 cm line, as this would require $mf_c \leq 0.002$. In the dense cores the weak 2 cm lines occur owing to the transition between absorption and emission. This transition occurs for any $X(H_2CO)$ at a characteristic density which is only weakly dependent upon temperature. In general, however, the 2 mm line observed is too weak at this characteristic density to fit the model. If $X(H_2CO)$ is constant at 10^{-9}, this characteristic density occurs at $n = 10^5$ cm^{-3} (Fig. 7). The corresponding 2 mm line would be over 5 K. Comparing this intensity with the observed strength, gives $mf_c = 0.25$. Models with lower densities and higher filling factors are incompatible with the large observed intensity of the higher frequency transitions (Table 4), which require high densities to be excited. Only the high-density, low H_2CO abundance models are acceptable for large filling factors. A more complex clump model might be made to fit the data, but the simple model incorporating uniform clumps suggests that abundance variations are required.

Of the alternative models describing the H_2CO line intensities at the cloud cores and their radial variations, the most compelling is one in which $X(H_2CO)$ decreases with density as the molecules are depleted onto grains. This simple picture for the rotational line emission is supported by photometric and polarimetric observations of stars in these clouds (Vrba *et al.* 1975; Carrasco, Strom, and Strom 1973; Vrba, Coyne, and Tapia 1981), which demonstrate the growth of grains with increasing extinction in the outer parts of the clouds. Evidence that the molecules, depleted from the gas phase, are found in grain mantles comes from the detection of an infrared absorption feature due to ice mantles on grains in the dense cold ρ Oph B core (Harris, Woolf, and Rieke 1978). Spectroscopic observations of infrared features in other clouds show the presence of solid phase NH_3 (Knacke *et al.* 1982) and H_2CO (Baas *et al.* 1983) on dust grains. The time scales for gas-grain collisions compared with the dynamical time scale of the cloud core, discussed below, favor accretion of molecules onto grains, where they are likely to remain in cold regions. These factors coupled to the simplicity of the model for the gas proposed here and its success in reproducing a wide range of cloud features make a compelling case that the shallow decline in integrated intensity of molecular emission lines, toward the dense cores of the molecular clouds, is a result of declining abundance as molecules accrete onto grains. In addition, the derived radial density variations accurately reflect those present within the cloud cores.

b) Comparison with the Density Profiles in Other Clouds

The radial density profile has previously been determined in only a few molecular clouds. Westbrook *et al.* (1976) and Cheung *et al.* (1980) have determined the density variation from observations of the 1 mm continuum emission from the dust associated with molecular clouds. The clouds that they observed (e.g., W3, OMC-1, Sgr B2, W49, and W33) are typically quite distant, and the spatial resolution that they achieved is poor. Unfortunately, as a result, data are available at the core and only two to three additional radial positions. Assuming a radial variation of grain temperature of $T_g(R) \propto R^{-0.4}$ to $R^{-0.5}$, they find $\rho(R) \propto R^{-1.5 \pm 0.5}$ for grains.

For the molecular component of the cloud, Wootten, Snell, and Evans (1980) have modeled the H_2CO and HCO^+ emission toward L1529, S255, and S140. Toward the cold dust cloud L1529 they observed the core position and three additional concentric rings; they found that the 2 cm and 2 mm H_2CO data were fitted by a rather shallow $\rho(R) \propto R^{-0.35}$ power law. Toward S140 and S255 they found that the H_2CO intensities could be modeled by a $\rho(R) \propto R^{-2}$ density variation. The dense cores of these clouds are similar in structure to those observed in ρ Oph and R CrA. Sandqvist and Bernes (1980) modeled the H_2CO observations in the cold cloud L1551 with a Monte Carlo simulation of the radiative transfer and a constant $X(H_2CO)$ to find a density variation of the form $\rho(R) \propto R^{-0.8}$.

Myers *et al.* (1978) have estimated the radial density profile in the ρ Oph cloud by a different technique than that used here. They compared the spatial extent of the molecular emission from a number of different molecules with the density required to excite the observed transitions. There are several potential problems with their method. First, many of the molecules (e.g., CO, ^{13}CO, HCO^+, and H) that they included in their study suffer self-absorption effects owing to high optical

depth, the importance of which was not fully recognized at that time. Self-absorption can systematically bias the determination of the spatial extent of molecular emission and also the measurement of line widths, which they also modeled. Furthermore, their single density profile combined results for four separate regions of the cloud, which were identified with four peaks in the map of 6 cm H_2CO absorption. Unfortunately, the 6 cm H_2CO line by itself is not a good indicator of the location of the high-density portions of any cloud. Because of the non–LTE population of the 6 cm and 2 cm H_2CO transitions at low densities, which produces absorption against the 3 K background, weak absorption lines are expected to occur at low densities and again at high densities when the transition changes from absorption to emission. The observations reported here confirm this expected behavior for the 2 cm line and for the 6 cm line by the fact that the positions of the two dense cores in our 2 mm H_2CO map lie at the positions of relative minimums (weak absorption) in the Myers *et al.* (1978) 6 cm H_2CO map. Despite these potential problems Myers *et al.* (1978) find a density variation that follows a $\rho(R) \propto R^{-1.3}$ law, consistent to within the errors with the results presented here for ρ Oph A. Furthermore, if the dense core that we observe were surrounded by a uniform low-density ($< 10^4$ cm^{-3}) envelope, the steepness of the core density variation law estimated by Myers *et al.* would be underestimated compared with our method.

c) *The Density Profile of a Star-Forming Cloud*

We have sought, in regions of recent star formation, dense cloud cores (which do not contain massive stars) whose density distribution should closely approximate that appropriate to the initial stages of the birth of a star. Future massive star formation may occur within these cores.

The dense cores observed in ρ Oph and R CrA have masses 20–100 $M_\odot$ and a measured density distribution of the form $\rho(R) \propto R^{-3/2}$ to R^{-2} over a range of projected radial distance from ~ 0.05 to 0.50 pc. The exact nature of future evolution of these clouds cannot be predicted, but formation of a massive star or fragmentation into a number of stars seems likely. A $n \propto R^{-2}$ density law is a natural consequence of the balancing of gravitational and pressure gradients in an isothermal self-gravitating cloud (Shu 1977). The collapse of such a cloud develops from this nearly equilibrium configuration and follows the self-similar collapse solutions found by Larson (1969, 1972). The outer nearly static envelope maintains a R^{-2} density distribution, while the inner region surrounding a centrally condensed object has a $R^{-3/2}$ density distribution characteristic of steady state accretion at the free-fall rate. Shu (1977) noted that the typical calculations of gravitational collapse choose boundary conditions appropriate to the formation of solar-mass stars. The mass assumed in these calculations can be scaled up to the collapse of large molecular clouds and may best describe the evolution of the more massive dense cores we observe in the ρ Oph and R CrA clouds.

The current data are not sufficiently accurate to distinguish the density profile of an isothermal equilibrium (R^{-2}) from a centrally condensed collapsing ($R^{-3/2}$) configuration. Heating sources exist in the surrounding cloud, so isothermal conditions may not occur. The near-infrared objects found near the ρ Oph B core have not yet succeeded in warming the densest part of the core above the point where the formation of DCO^+ is favored. In addition, the lack of far-infrared emission suggests that massive star formation has not yet begun. Is future star formation in ρ Oph B or the two other dense cores inevitable, or can they be supported against collapse by turbulence, rotation, or magnetic fields? Equating the gravitational energy and the rotational energy, the critical velocity, at the equator, required to equatorially stabilize the cloud against collapse would be $V_R = (3GM/R)^{1/2}$. A value of $V_{\rm TURB} = (6GM/5R)^{1/2}$ would be appropriate for turbulent support. Table 5 compares the calculated critical rotational velocity for each of the three cloud cores with the observed line widths of the 2 mm H_2CO transition. This line is most likely saturated and broader than that produced by the actual velocity field of the cloud. Even so, in all three cases the H_2CO lines are too narrow to indicate sufficient support from either rotation or turbulence to prevent collapse. In both the ρ Oph and R CrA clouds the dust and gas distributions are elongated along the direction of the optical polarization of visible stars (Vrba, Strom, and Strom 1976*b*), suggesting that magnetic fields have played a significant role in cloud evolution. Vrba, Coyne, and Tapia (1981) find that the magnetic field needed to produce the observed grain alignment in R CrA is $B(\mu\text{G}) = 13\ [n(\text{cm}^{-3})]^{0.38}$ in the outer part of the cloud where $n < 10^3$ cm^{-3}. In the higher density portions of the cloud the observations indicate that B approaches a constant value of 150 μG. This could be partially explained by the insensitivity of polarization measurements to large B-values that might occur in the dense parts of the cloud where the gas and dust temperatures are nearly equal and grain alignment is less effective. It may also be true that the maximum magnetic field reaches only ~ 150 μG in the cloud core since Vrba *et al.* find that the mass spectra of stars formed in the cloud would be inconsistent with B much greater or lower than 150 μG. A large B-value would have prevented the formation of the observed stars, and too many low-mass stars would have formed if B were lower. The magnetic field required to stabilize the cloud from collapse would be $B = 0.2\ M(M_\odot)/R^2$ (pc) (Lequeux 1977). For the R CrA cloud this requires 1400 μG, an order of magnitude greater than the inferred value of 150 μG. Only if extrapolation of the scaling law given by Vrba *et al.* were appropriate in the dense core

TABLE 5

CLOUD CORES

Parameter	ρ Oph A	ρ Oph B	R CrA
Core radius (pc)	0.09	0.08	0.06
Core density (cm^{-3})	3×10^5	10^6	4×10^5
Core mass ($M_\odot$)	50	110	19
Required line width for rotational stabilization ($km\ s^{-1}$)	2.5	4.1	2.0
Observed line width in core ($km\ s^{-1}$)	1.1	1.0	1.6
Free-fall time scale (yr)	6.4×10^4	3.5×10^4	5.6×10^4

would values of B be comparable to that required to stabilize the core. The magnetic field may slow collapse, but the star formation that has occurred in the ρ Oph and R CrA clouds attests to the inability of the magnetic fields to prevent collapse.

If the clouds' evolution approximates free-fall collapse, the time scale can be determined. The free-fall time (Lequeux 1977) is $t_{ff} = (3\pi/32G\rho)^{1/2} = 1.65\times10^7\ [R^3\ (\mathrm{pc})/M\ (M_\odot)]^{1/2}$ yr. From the observed size and mass, the free-fall time is 6×10^4 yr for ρ Oph A, 3.5×10^4 yr for ρ Oph B, and 6×10^4 yr for R CrA. Collapse may well be retarded but not halted by the effects of turbulence (Scalo and Pumphrey 1982), rotation, and magnetic fields; and the actual evolutionary time scale will be longer than the free-fall time scale.

In many respects ρ Oph B resembles cold dark clouds like L134N and L1534; any star which has formed within these cores has lacked either the capacity or the time to heat the core. Because its density is two orders of magnitude greater, the cold massive ρ Oph B core may be on the threshold of massive star formation.

VII. CONCLUSIONS

We find that the dense cores of molecular clouds, on the threshold of star formation, can be characterized by steep density gradients of the form $\rho(R) \propto R^{-3/2}$ to R^{-2}. As the density increases, the H_2CO abundance decreases as gas phase molecules condense onto grains. Neither the observed rotation, turbulence, or magnetic fields are adequate to prevent collapse, suggesting that eventually further star formation will occur.

We wish to thank Lee Mundy for assistance with some of the observations and for helpful discussions. Receiver development at the University of Massachusetts is supported by NSF. This work was supported by NSF grant AST 81-16403 to The University of Texas at Austin, AST 81-16863 to the California Institute of Technology, and the Swedish Natural Science Research Council.

REFERENCES

Aannestad, P. A. 1973, *Ap. J. Suppl.*, **25**, 205.
Baas, F., Allamandola, L. J., Geballe, T. R., Persson, S. E., and Lacy, J. H. 1983, *Ap. J.*, **265**, 290.
Bernes, C., and Sandqvist, Aa. 1977, *Ap. J.*, **217**, 71.
Blades, J. C., and Whittet, D. C. B. 1980, *M.N.R.A.S.*, **191**, 701.
Brown, R. L., Gammon, R. H., Knapp, G. R., and Balick, B. 1974, *Ap. J.*, **192**, 607.
Brown, R. L., and Zuckerman, B. 1975, *Ap. J. (Letters)*, **202**, L125.
Carrasco, L., Strom, S. E., and Strom, K. M. 1973, *Ap. J.*, **182**, 95.
Cheung, L. H., Frogel, J. A., Gezari, D. Y., and Hauser, M. G. 1980, *Ap. J.*, **240**, 74.
de Muizon, M., Rouan, D., Lena, P., Nicollier, C., and Wijnbergen, J. 1980, *Astr. Ap.*, **83**, 140.
Elias, J. H. 1978, *Ap. J.*, **224**, 453.
Encrenaz, P. J., Falgarone, E., and Lucas, R. 1975, *Astr. Ap.*, **44**, 73.
Erickson, N. R. 1981, *IEEE Trans.*, **MTT-29**, 557.
Evans, N. J., II, and Kutner, M. L. 1976, *Ap. J. (Letters)*, **204**, L131.
Evans, N. J., II, Zuckerman, B., Sato, T., and Morris, G. 1975, *Ap. J.*, **199**, 883.
Falgarone, E., and Gilmore, W. S. 1981, *Astr. Ap.*, **95**, 32.
Fazio, G. G., Wright, E. L., Zeilik, M., II, and Low, F. T. 1976, *Ap. J. (Letters)*, **206**, L165.
Grasdalen, G., Strom, K. M., and Strom, S. E. 1973, *Ap. J. (Letters)*, **184**, L53.
Green, S., Garrison, B. J., Lester, W. A., Jr., and Miller, W. H. 1978, *Ap. J. Suppl.*, **37**, 321.
Harris, D. H., Woolf, N. J., and Rieke, G. H. 1978, *Ap. J.*, **226**, 829.
Harvey, P. M., Campbell, M. F., and Hoffman, W. 1979, *Ap. J.*, **228**, 445.
Herbig, G. H. 1960, *Ap. J. Suppl.*, **4**, 337.
Ho, P. T. P. 1977, Ph.D. thesis, Massachusetts Institute of Technology.
Knacke, R. F., McCorkle, S., Puetter, R. C., Erickson, E. F., and Kratsher, W. 1982, *Ap. J.*, **260**, 141.
Knacke, R. F., Strom, K. M., Strom, S. E., Young, E. and Kunkel, W. 1973, *Ap. J.*, **179**, 847.
Kutner, M. L., Evans, N. J., II, and Tucker, K. D. 1976, *Ap. J.*, **209**, 452.
Kutner, M. L., and Ulich, B. L. 1981, *Ap. J.*, **250**, 341.
Lada, C. J., and Wilking, B. A. 1980, *Ap. J.*, **238**, 620.
Larson, R. B. 1969, *M.N.R.A.S.*, **145**, 271.

Larson, R. B. 1972, *M.N.R.A.S.*, **157**, 121.
Lequeux, J. 1977, in *IAU Symposium 75, Star Formation*, ed. T. de Jong and A. Maeder (Dordrecht: Reidel), p. 69.
Linke, R. A., and Goldsmith, P. F. 1980, *Ap. J.*, **235**, 437.
Loren, R. B. 1979, *Ap. J.*, **227**, 832.
Loren, R. B., Evans, N. J., II, and Knapp, G. R. 1979, *Ap. J.*, **234**, 932.
Loren, R. B., and Wootten, A. 1983, in preparation.
Loren, R. B., Wootten, R. B., Mundy, L. G., Sandqvist, Aa., Peters, W. L., III, and Vanden Bout, P. A. 1983, in preparation.
Loren, R. B., Wootten, A., Sandqvist, Aa., and Bernes, C. 1980, *Ap. J.* (*Letters*), **240**, L165.
Marraco, H. G., and Rydgren, A. E. 1981, *A.J.*, **86**, 62.
Myers, P. C., Ho, P. T. P., Schneps, M. H., Chin, G., Pankonin, V., and Winnberg, A. 1978, *Ap. J.*, **220**, 864.
Plambeck, R. L., and Williams, D. R. W., 1979, *Ap. J.* (*Letters*), **227**, L43.
Sandqvist, Aa., and Bernes, C. 1980, *Astr. Ap.*, **89**, 187.
Scalo, J. M., and Pumphrey, W. A. 1982, *Ap. J.* (*Letters*), **258**, L29.
Shu, F. H. 1977, *Ap. J.*, **214**, 488.
Snell, R. L. 1981, *Ap. J. Suppl.*, **45**, 121.
Snell, R. L., Loren, R. B., and Plambeck, R. L. 1980, *Ap. J.* (*Letters*), **239**, L17.
Soifer, B. T., Russell, R. W., and Merrill, K. M. 1976, *Ap. J.* (*Letters*), **207**, L83.
Strom, K. M., Strom, S. E., and Grasdalen, G. L. 1974, *Ap. J.*, **191**, 111.
Strom, S. E., Strom, K. M., Yost, J., Carrasco, L., and Grasdalen, G. 1972, *Ap. J.*, **173**, 353.
Vrba, F. J., Coyne, G. V., and Tapia, S. 1981, *Ap. J.*, **243**, 489.
Vrba, F. J., Strom, K. M., Strom, S. E., and Grasdalen, G. L. 1975, *Ap. J.*, **197**, 77.
Vrba, F. J., Strom, S. E., and Strom, K. M., 1976*a*, *A.J.*, **81**, 317.
_____. 1976*b*, *A.J.*, **81**, 958.
Watson, W. D., and Salpeter, E. E. 1972, *Ap. J.*, **175**, 659.
Westbrook, W. E., Werner, M. W., Elias, J. H., Gerzari, D. Y., Hanser, M. G., Lo, K. Y., and Neugebauer, G. 1976, *Ap. J.*, **209**, 94.
White, R. E. 1977, *Ap. J.*, **211**, 744.
Whittet, D. C. B. 1974, *M.N.R.A.S.*, **168**, 371.
Wilking, B. A., and Lada, C. J. 1982, preprint.
Willner, S. P., Russell, R. W., Puetter, R. C., Soifer, B. T., and Harvey, P. M. 1979, *Ap. J.* (*Letters*), **229**, L65.
Wootten, A., Evans, N. J., II, Snell, R. L., and Vanden Bout, P. A. 1978, *Ap. J.* (*Letters*), **225**, L143.
Wootten, A., Loren, R. B., and Snell, R. L. 1982, *Ap. J.*, **255**, 160.
Wootten, A., Snell, R. L., and Evans, N. J., II. 1980, *Ap. J.*, **240**, 532.

ROBERT B. LOREN: Millimeter Wave Observatory, McDonald Observatory, Ft. Davis, TX 79734

AA. SANDQVIST: Stockholm Observatory, S-133 00 Saltsjöbaden, Sweden

ALWYN WOOTTEN: National Radio Astronomy Observatory, Charlottesville, VA 22901